Neuron

Report

Stress undermines reward-guided cognitive performance through synaptic depression in the lateral habenula

Graphical Abstract

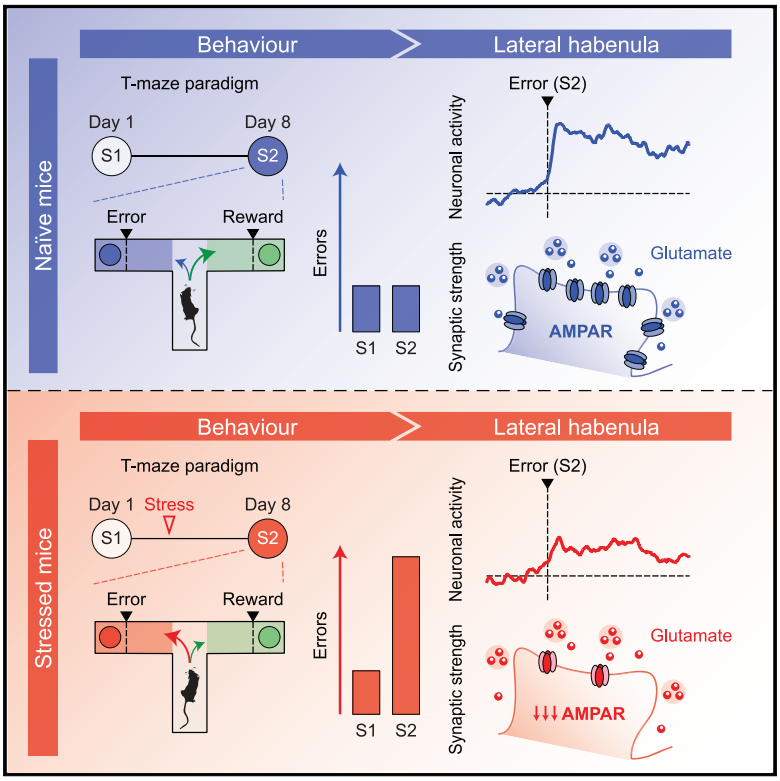

Highlights

- A specific phase during an appetitive cognitive task engages LHb neuronal dynamics
- The strength of excitatory synapses in LHb neurons predicts cognitive performance
- Stress triggers cognitive impairments and disrupts LHb neuronal activity
- Deficits in reward-guided behaviors require a decrease in LHb AMPAR transmission

Authors

Alvaro Nuno-Perez, Massimo Trusel, Arnaud L. Lalive, ..., Mariano Soiza-Reilly, Claudia Bagni, Manuel Mameli

Correspondence

manuel.mameli@unil.ch

In Brief

Effective evaluation of costs and benefits is fundamental for survival and vulnerable to stress. Nuno-Perez et al. show that the strength of AMPAR transmission within the mouse lateral habenula governs the incidence of non-rewarded choices in a reward-guided task. Stress weakens habenular excitatory synapses and consequently augments non-rewarded decisions.

Nuno-Perez et al., 2021, Neuron *109*, 947–956
March 17, 2021
https://doi.org/10.1016/j.neuron.2021.01.008

CellPress

Neuron

CellPress
OPEN ACCESS

Report

Stress undermines reward-guided cognitive performance through synaptic depression in the lateral habenula

Alvaro Nuno-Perez,[1] Massimo Trusel,[1] Arnaud L. Lalive,[1] Mauro Congiu,[1] Denise Gastaldo,[1] Anna Tchenio,[1] Salvatore Lecca,[1] Mariano Soiza-Reilly,[2] Claudia Bagni,[1] and Manuel Mameli[1,3,4,*]

[1]The Department of Fundamental Neuroscience, The University of Lausanne, 1005 Lausanne, Switzerland
[2]IFIBYNE, The University of Buenos Aires, Buenos Aires, Argentina
[3]Inserm, UMR-S 839, 75005 Paris, France
[4]Lead contact
*Correspondence: manuel.mameli@unil.ch
https://doi.org/10.1016/j.neuron.2021.01.008

SUMMARY

Weighing alternatives during reward pursuit is a vital cognitive computation that, when disrupted by stress, yields aspects of neuropsychiatric disorders. To examine the neural mechanisms underlying these phenomena, we employed a behavioral task in which mice were confronted by a reward and its omission (i.e., error). The experience of error outcomes engaged neuronal dynamics within the lateral habenula (LHb), a subcortical structure that supports appetitive behaviors and is susceptible to stress. A high incidence of errors predicted low strength of habenular excitatory synapses. Accordingly, stressful experiences increased error choices while decreasing glutamatergic neurotransmission onto LHb neurons. This synaptic adaptation required a reduction in postsynaptic AMPA receptors (AMPARs), irrespective of the anatomical source of glutamate. Bidirectional control of habenular AMPAR transmission recapitulated and averted stress-driven cognitive deficits. Thus, a subcortical synaptic mechanism vulnerable to stress underlies behavioral efficiency during cognitive performance.

INTRODUCTION

The willingness to obtain a reward prompts goal-directed behaviors whose execution relies on the online deployment of cognitive processes (Halassa and Kastner, 2017). Events compromising the homeostatic state of individuals, defined here as stress, imperil such reward-guided cognitive capacities (Friedman et al., 2017). The prefrontal cortex contributes to cognitive functions, yet how subcortical neuronal systems govern these aspects in physiological and pathological conditions remains elusive (Arnsten, 2015).

The epithalamic lateral habenula (LHb) conveys reward and aversive signals to monoaminergic brain centers, including the mesolimbic dopamine system (Lecca et al., 2014; Matsumoto and Hikosaka, 2007). LHb neurons participate in cognitive processes by shaping decision-making and retrieval of spatial memories (Baker et al., 2015; Mathis et al., 2015; Stopper and Floresco, 2014). Importantly, lesion or pharmacological manipulations of the habenular complex suggest a role for the LHb in guiding choice selection during cognitive performance (Baker et al., 2017; Lecourtier et al., 2004; Thornton and Evans, 1984). For instance, upon the modification of environmental contingencies, perturbing habenular function prevents rodents from updating their decisions in a T-maze paradigm (Nielson and McIver, 1966). Hence, LHb neurons integrate a range of internal and external information to support fitness during cognitive performance.

Exposure to stressors aberrantly increases neuronal activity, promotes long-lasting synaptic adaptations, and induces transcriptional remodeling within the LHb (Cerniauskas et al., 2019; Cui et al., 2018; Lecca et al., 2016; Li et al., 2011). These cellular alterations are instrumental for the emergence of behavioral phenotypes typical of mood disorders (Hu et al., 2020). Stress can concomitantly drive suboptimal decision-making, a hallmark of neuropsychiatric conditions such as anxiety and depression (Friedman et al., 2017; Schwabe and Wolf, 2009; Sousa and Almeida, 2012). However, whether causality exists between neuronal plasticity within the LHb and stress-driven cognitive deficits remains to be addressed.

Here, we combined photometric analysis of calcium signals, slice electrophysiology, and LHb-specific manipulations of excitatory synaptic transmission to establish that (1) LHb neurons participate in a distinct phase of an appetitive task associated with a negative outcome, (2) habenular synaptic strength is predictive for cognitive performance, and (3) stress-driven synaptic depression in LHb neurons is instrumental for the expression of cognitive deficits.

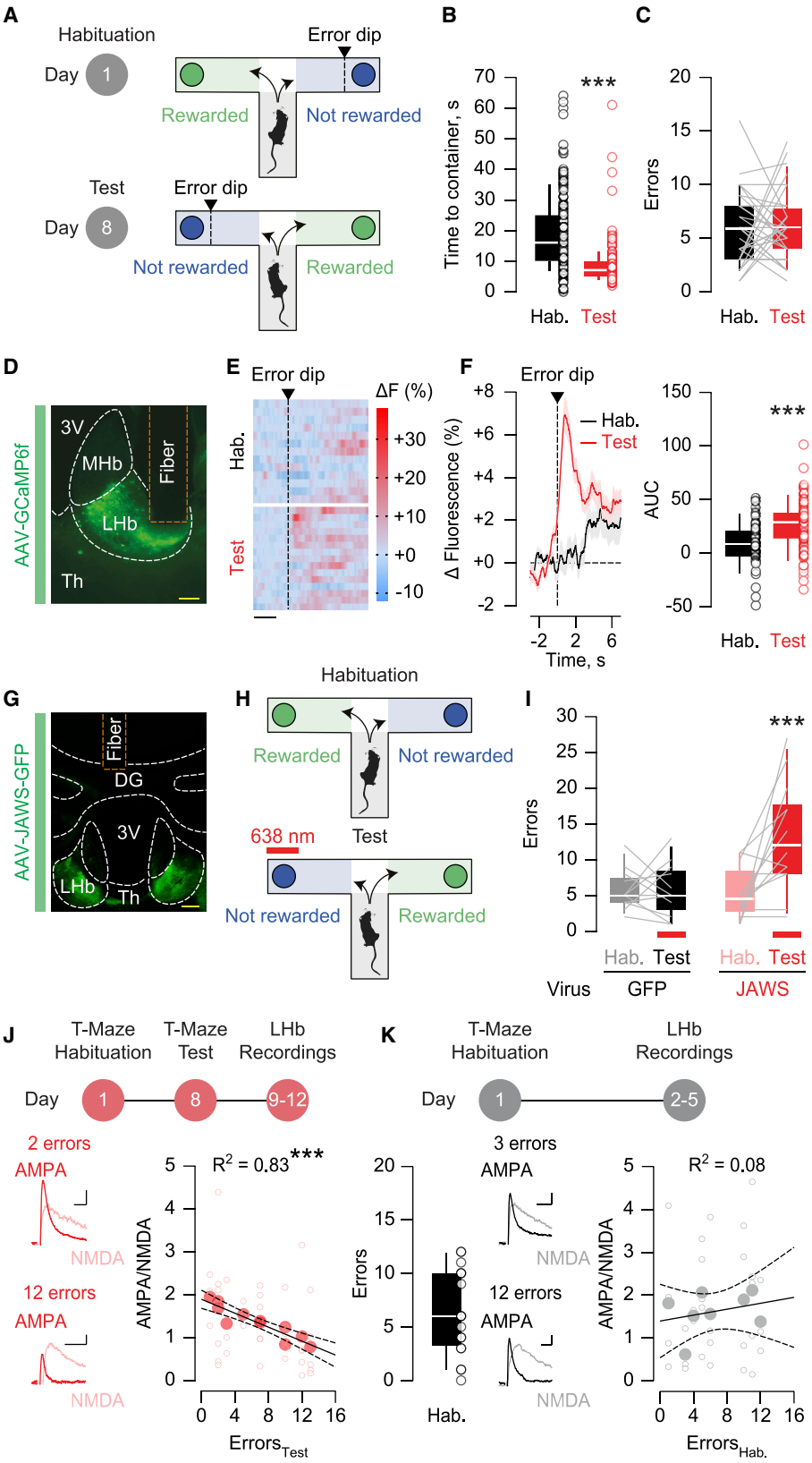

(legend on next page)

RESULTS

Excitatory transmission onto LHb neurons as a substrate for cognitive performance

We designed a reward-guided task using a T-maze paradigm in which food-restricted mice choose between two alternative arms throughout consecutive trials (Friedman et al., 2017). One arm was systematically baited with a food reward (chow, 10 mg), whereas the opposite remained non-baited. Mice were first exposed to the T-maze during the habituation session (day 1) and re-exposed one week later during the test session (day 8), when arm outcomes were inverted (Figure 1A). Sessions were terminated whenever mice chose the rewarded arm 5 consecutive times, or after 35 trials if the completion criterion was not attained. Mice reached the container located at the end of the arms more rapidly during the test session compared with habituation, suggesting the emergence of a goal-directed behavior (Figure 1B). The performance, as measured by the number of head dips into the non-rewarded container (henceforth errors), was comparable across sessions (Figure 1C). Therefore, mice coped efficiently with the switch in outcome position. Moreover, the distribution and preference of reward choices were similar during habituation and the test session (Figures S1A–S1D), suggesting that mice did not simply develop a strategy to avoid the session termination and maximize caloric intake.

The LHb participates in cognitive processes, as well as the encoding of reward omission, but whether specific phases of the T-maze paradigm engage LHb neurons is unknown (Matsumoto and Hikosaka, 2007; Stopper and Floresco, 2014). To test this, we injected a GCaMP6f-expressing adeno-associated virus (AAV; $rAAV_{2.5}$-hSyn1-GCaMP6f) in the LHb to monitor population calcium dynamics with fiber photometry (Figures 1D, S1E, and S1F) (Cui et al., 2014). After increasing the number of trials within a session for analytical and statistical purposes (see STAR Methods), we detected LHb fluorescence transients time-locked to head dips into the non-rewarded container (Figures 1E and 1F). Such calcium signals emerged during early trials of the test session and were smaller in the absence of arm switch (Figures S1G and S1H). In contrast, reward dips led to comparable fluorescence changes across sessions (Figures S1I and S1J). The dichotomy between transients recorded after error and reward dips was conserved when calcium signals were aligned to entry into the respective arms (Figures S1K and S1L). Finally, optical silencing of LHb neurons ($rAAV_8$-hSyn1-JAWS-GFP), which was time locked to error dips during the test session, increased the error incidence compared with control animals (Figures 1G–1I and S1M–S1P). Hence, a distinct phase associated with a negative outcome recruits timely LHb neuronal activity to instruct choice selection during the reward-guided task.

The LHb is defined as a disappointment brain center, and synaptic adaptations of excitatory transmission within this nucleus underlie behaviors in response to negative experiences (Shabel et al., 2019; Trusel et al., 2019). We thereby examined the strength of excitatory synaptic transmission in LHb neurons, after mice experienced reward and error outcomes in the T-maze task. We prepared LHb-containing acute slices and recorded AMPA/NMDA ratios (AMPA/NMDA) as a proxy for postsynaptic efficacy after the test session at day 8 (Lüthi and Lüscher, 2014). The analysis revealed a negative correlation between number of errors performed at day 8 and AMPA/NMDA (Figure 1J). Such a correlation was absent when AMPA/NMDA was recorded after the habituation session (Figure 1K). Altogether, these data demonstrate that encountering the non-rewarded outcome recruits LHb neurons and that excitatory synaptic strength at LHb synapses is predictive for mouse performance in the reward-guided task.

Stress drives cognitive deficits and weakens habenular excitatory transmission

A stressful experience leads to maladaptive shifts in cognitive performance and triggers plasticity of excitatory synaptic transmission in LHb neurons (Friedman et al., 2017; Li et al., 2011). We employed a stressful challenge known to perturb LHb function by subjecting mice to a single session of unpredictable foot shocks one day after the habituation session of the T-maze

Figure 1. Excitatory transmission onto LHb neurons guides cognitive performance during the T-maze task

(A) Schematic of the behavioral paradigm.

(B) Boxplots and scatterplots of the time to reach the arm containers (habituation, black: n = 28 mice/140 trials, 20.02 ± 1.006; test session, red: n = 29 mice/144 trials, 8.688 ± 0.5951). Mann-Whitney test (U = 2,602, ***p < 0.001).

(C) Boxplots and scatterplots of the error incidence (habituation, black: n = 31 mice, 5.839 ± 0.6258; test session, red: n = 31 mice, 6.29 ± 0.5888).

(D) Representative injection site of AAV-GCaMP6f and fiber implantation (scale bar: 100 μm). 3V, third ventricle; M/LHb, medial/lateral habenula; Th, thalamus.

(E) Single-mouse heatmap of LHb fluorescence aligned to entry into the non-rewarded container (error dip; scale bar: 2 s).

(F) Time course of the average LHb fluorescence aligned to entry into the non-rewarded container (error dip). Boxplots and scatterplots of the area under the curve (AUC) (habituation, black: n = 5 mice/40 trials, 8.191 ± 3.429; test session, red: n = 5 mice/74 trials, 25.86 ± 2.758). Mann-Whitney test (U = 830, ***p < 0.001).

(G) Representative injection site of AAV-JAWS and fiber implantation (scale bar: 200 μm). DG, dentate gyrus.

(H) Schematic of the behavioral paradigm. Red light during the test session, aligned to entry into the non-rewarded container.

(I) Boxplots and scatterplots of the error incidence in GFP mice (black: n = 12 mice, 5.75 ± 0.7739 during habituation and 5.75 ± 1.021 during test) and JAWS mice (red: n = 13 mice, 5.154 ± 0.972 during habituation and 13 ± 2.044 during test). Two-way repeated-measure ANOVA ($F_{1,23}$ = 8.306) with Sidak correction (***p < 0.001, habituation versus test).

(J) Experimental timeline. Example traces of AMPA/NMDA after the test session (scale bars: 10 pA and 10 ms). Correlation plot between AMPA/NMDA and error incidence of the test session (open circles: individual values; closed circles: single-mouse averages; n = 11 mice/43 cells). Pearson correlation (R^2 = 0.833, $F_{1,9}$ = 44.89, ***p < 0.001).

(K) Experimental timeline. Boxplots and scatterplots of the error incidence during habituation (n = 16 mice, 5.313 ± 0.7113). Example traces of AMPA/NMDA after habituation (scale bars: 10 pA and 5 ms). Correlation plot between AMPA/NMDA and error incidence during habituation (open circles: individual values; closed circles: single-mouse averages; n = 8 mice/33 cells). Pearson correlation (R^2 = 0.0838, $F_{1,6}$ = 0.5486, p = 0.487).

Data are represented with heatmaps, boxplots (median and quartiles), or mean ± SEM. See also Figure S1.

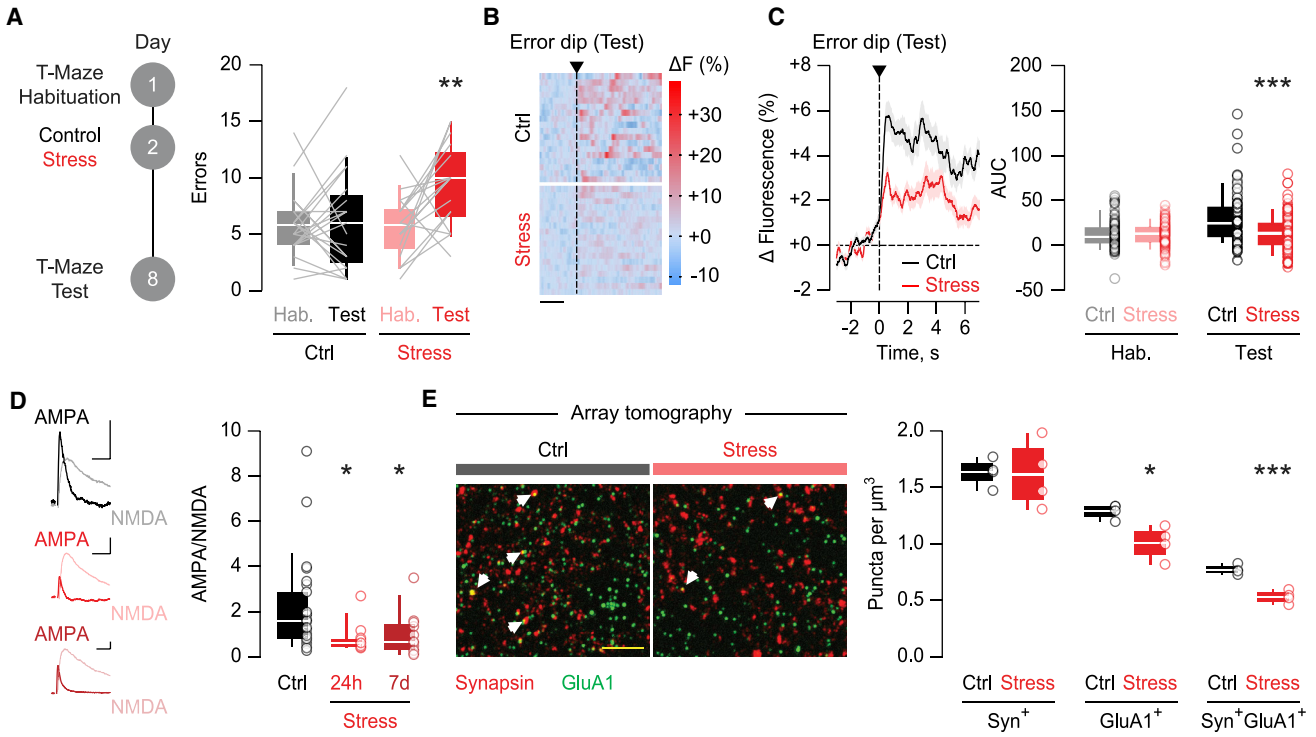

Figure 2. Stress triggers cognitive deficits and reduces AMPAR transmission in LHb neurons

(A) Experimental timeline. Boxplots and scatterplots of the error incidence (control, black: n = 20 mice, 5.8 ± 0.6633 during habituation and 6.05 ± 1.006 during test; stress, red: n = 17 mice, 5.706 ± 0.6847 during habituation and 9.353 ± 0.895 during test). Two-way repeated-measure ANOVA ($F_{1,35}$ = 6.297) with Sidak correction (**p < 0.01, habituation versus test).

(B) Single-mouse heatmap of LHb fluorescence aligned to entry into the non-rewarded container (error dip) during the test session (scale bar: 2 s).

(C) Time course of the average LHb fluorescence aligned to entry into the non-rewarded container (error dip) during the test session. Boxplots and scatterplots of the AUC (control, black: n = 5 mice/69 trials, 12.549 ± 1.987 during habituation; n = 5 mice/76 trials, 30.331 ± 3.363 during test; stress, red: n = 5 mice/70 trials, 12.276 ± 1.57 during habituation; n = 5 mice/91 trials, 14.841 ± 2.144 during test). Two-way ANOVA ($F_{1,302}$ = 10.56) with Sidak correction (***p < 0.001, control versus stress).

(D) Example traces of AMPA/NMDA (scale bars: 30 pA and 10 ms). Boxplots and scatterplots of AMPA/NMDA (control, black: n = 6 mice/26 cells, 2.105 ± 0.4023; stress, light red: 24 h, n = 4 mice/13 cells, 0.76 ± 0.1717; dark red: 7 days, n = 3 mice/12 cells, 0.9567 ± 0.2753). One-way ANOVA ($F_{2,48}$ = 4.042) with Holm-Sidak correction (*p < 0.05, comparisons against control).

(E) Array tomography images obtained from single 100-nm slices immunolabeled against Synapsin (red) and GluA1 (green) (scale bar: 5 μm). White arrows indicate representative puncta showing co-localization of both markers. Boxplots and scatterplots of the number of puncta per cubic micrometer (control, black: n = 4 mice, 1.633 ± 0.0615 for Synapsin, 1.289 ± 0.0319 for GluA1 and 0.769 ± 0.0207 for Synapsin/GluA1; stress, red: n = 4 mice, 1.616 ± 0.1474 for Synapsin, 1.01 ± 0.0723 for GluA1 and 0.5303 ± 0.0282 for Synapsin/GluA1). Unpaired Student's t test (GluA1: t_6 = 3.525, *p < 0.05; Synapsin/GluA1: t_6 = 6.828, ***p < 0.001). Data are represented with heatmaps, boxplots (median and quartiles), or mean ± SEM. See also Figures S2 and S3.

task (Stamatakis and Stuber, 2012). One week later, mice performed a greater number of errors during the test session, in contrast with control animals (Figure 2A). Accordingly, stress-exposed mice shifted their choice from reward-to-reward toward reward-to-error transitions (Figures S2A and S2B). Moreover, mice from all experimental groups reached the container located at the end of the arms more rapidly during the test session (Figure S2C), suggesting that a stressful experience compromises reward-guided behaviors without affecting the motivational component. The cognitive deficits following stress exposure, together with the result of the optical silencing of LHb neurons (Figure 1I), leads to the prediction that stress disrupts LHb calcium dynamics during head dips into the non-rewarded container. Indeed, compared with control animals, stress-exposed mice exhibited smaller fluorescence transients aligned to error dips during the test session (Figures 2B, 2C, S2D, and S2E). The extent of calcium signals negatively correlated with single-mouse error incidence (Figure S2F). Altogether, these results suggest that stress concomitantly impairs reward-guided behaviors and error-driven LHb neuronal activity.

Inspired by the negative correlation between error incidence and AMPA/NMDA in the LHb (Figure 1J), we hypothesized that stress-exposed mice would exhibit weaker excitatory synaptic transmission than their control counterparts. AMPA/NMDA from LHb neurons diminished in acute brain slices prepared 24 h and 7 days after stress exposure (Figure 2D). Generalizing this finding to stressors of a different nature, AMPA/NMDA decreased similarly 24 h after a single session of restraint stress (Figure S3A). To identify the expression mechanism of this plasticity, we employed quantitative array tomography to visualize habenular AMPA receptors (AMPARs; GluA1) and NMDA receptor (NMDAR) subunits (GluN1). Stress decreased the density of synaptic GluA1

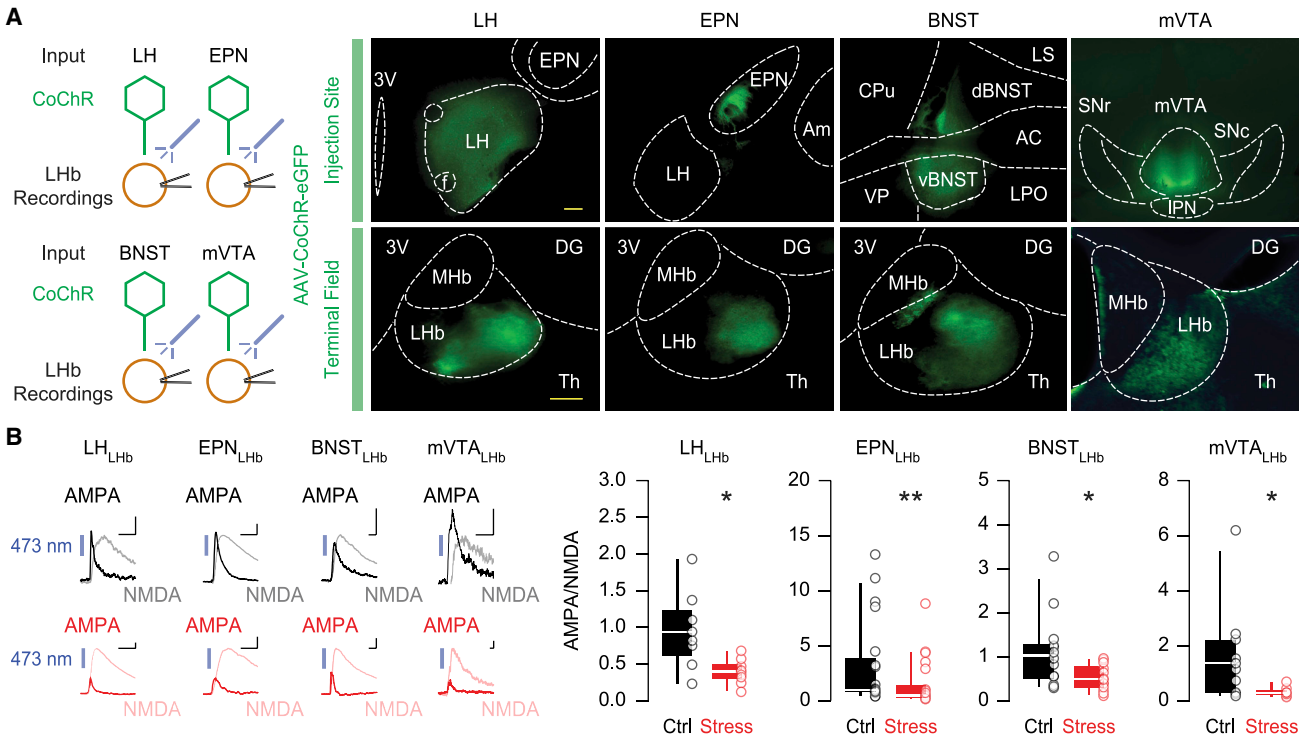

Figure 3. Stress-driven depression of habenular AMPAR transmission is not input-specific

(A) Schematic of the experimental design. Representative injection sites of AAV-CoChR (top, scale bar: 200 μm) and the corresponding terminal field within the LHb (bottom, scale bar: 100 μm). LH, lateral hypothalamus; f, fornix; EPN, entopeduncular nucleus; Am, amygdala; CPu, caudate putamen; VP, ventral pallidum; LS, lateral septum; d/vBNST, dorsal/ventral bed nucleus of the stria terminalis; AC, anterior commissure; LPO, lateral preoptic area; SNr/c, substantia nigra pars reticulata/compacta; mVTA, medial ventral tegmental area; IPN, interpeduncular nucleus.

(B) Example traces of input-specific AMPA/NMDA (scale bars: 50 pA and 10 ms for LH, EPN, and BNST; 10 pA and 10 ms for mVTA). Boxplots and scatterplots of AMPA/NMDA (control, black: LH, n = 2 mice/8 cells, 0.9538 ± 0.1864; EPN, n = 5 mice/20 cells, 3.164 ± 0.8938; BNST, n = 4 mice/13 cells, 1.102 ± 0.235; mVTA, n = 3 mice/10 cells, 1.633 ± 0.5646; stress, red: LH, n = 3 mice/9 cells, 0.3944 ± 0.0559; EPN, n = 7 mice/22 cells, 1.431 ± 0.4577; BNST, n = 5 mice/13 cells, 0.5162 ± 0.0799; mVTA, n = 2 mice/8 cells, 0.3113 ± 0.0636). Mann-Whitney test (LH: U = 10; EPN: U = 110; BNST: U = 41.5; mVTA: U = 12.5) (**p < 0.01, *p < 0.05). Data are represented with boxplots (median and quartiles) or mean ± SEM. See also Figure S3.

without affecting GluN1 puncta, pointing to AMPAR downscaling as the main underlying mechanism for stress-induced AMPA/NMDA reduction (Figures 2E and S3B). Reinforcing this idea, stress lowered AMPA/NMDA and AMPAR currents evoked by single-photon (S)-α-Amino-2,3-dihydro-4-methoxy-7-nitro-δ-oxo-1H-indole-1-pentanoic acid (MNI)-glutamate uncaging, as well as the frequency and amplitude of AMPAR, but not NMDAR, excitatory postsynaptic currents (EPSCs) (Figures S3C–S3E). Finally, stress decreased the AMPAR rectification index and sensitivity to the GluA2-lacking AMPAR blocker NASPM without affecting currents evoked by stimulation with high-frequency trains (Figures S3F–S3H). Thus, although we cannot rule out changes in NMDAR transmission, a stressful experience produces maladaptive reward-guided behaviors, together with a postsynaptic reduction in GluA1 AMPAR at LHb synapses.

Circuit basis of stress-driven AMPAR plasticity

We next examined whether stress-driven synaptic depression follows a circuit-specific rule or occurs widely throughout the LHb. LHb neurons receive glutamatergic inputs from different brain regions, including the lateral hypothalamus (LH), the entopeduncular nucleus (EPN) of the basal ganglia, the bed nucleus of the stria terminalis (BNST), and the medial ventral tegmental area (mVTA) (Lazaridis et al., 2019; Root et al., 2014; Shabel et al., 2012; Stamatakis et al., 2016). To investigate input-specific efficacy of glutamatergic neurotransmission, we independently injected a *Chloromonas oogama* channelrhodopsin (CoChR)-encoding AAV (rAAV$_{2.5}$-hSyn1-CoChR-eGFP) in the LH, EPN, BNST, or mVTA (Figure 3A) (Trusel et al., 2019). Recording input-specific AMPA/NMDA in the LHb revealed a reduction in synaptic strength at all inputs probed 24 h after stress exposure (Figure 3B). Input-specific stimulation with high-frequency trains displayed no alteration in presynaptic function at any input except for the mVTA, which reflected a reduction in release probability following stress exposure (Figure S3I) (Cerniauskas et al., 2019). Therefore, a stressful experience weakens AMPAR transmission onto LHb neurons, regardless of the anatomical source of glutamate.

Establishing causality between stress-driven synaptic depression and cognitive deficits

Is the stress-driven weakening of habenular excitatory transmission required for the increased error incidence in the T-maze task? Initially, we aimed to emulate the stress-driven synaptic

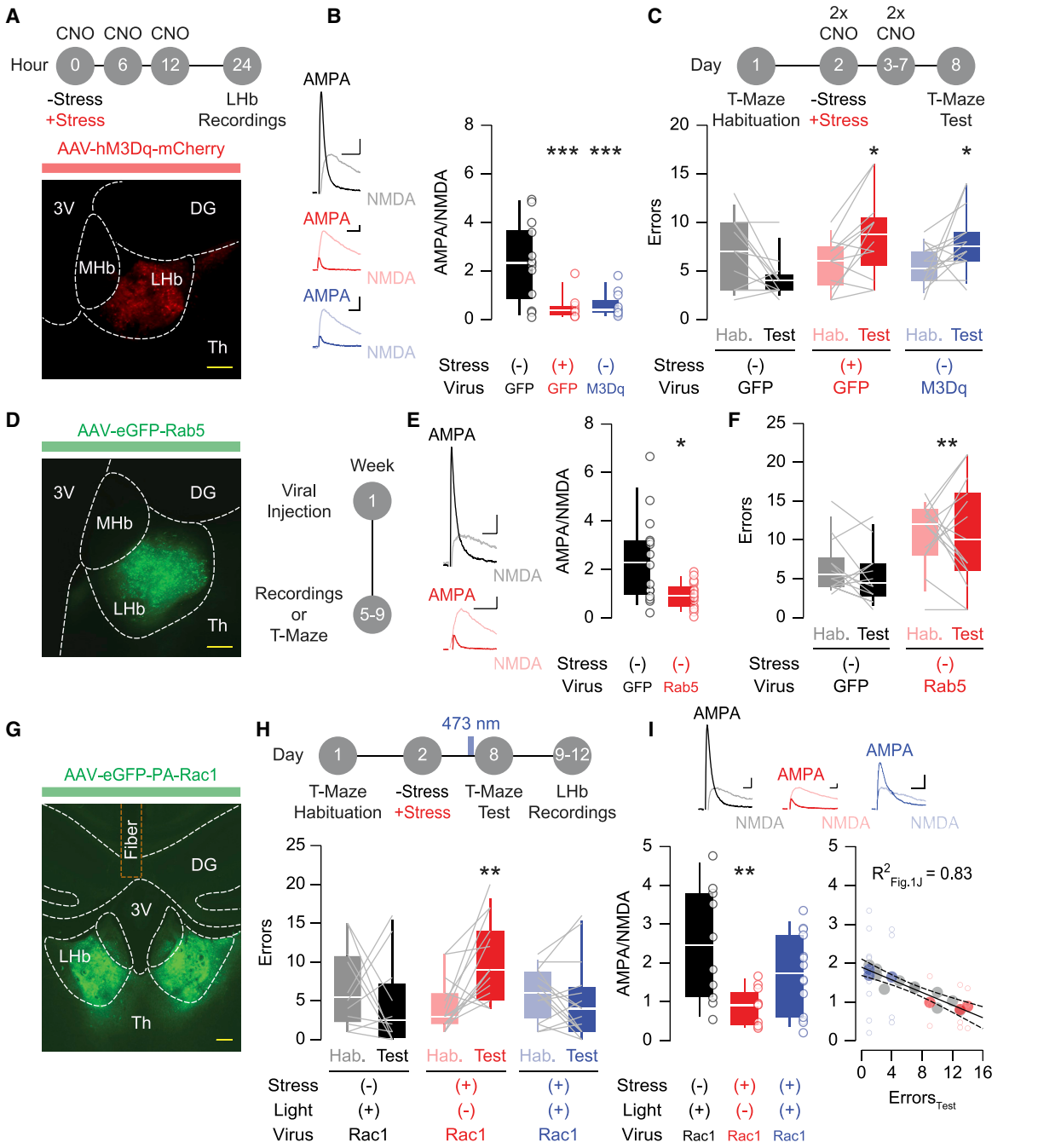

Figure 4. Reduction and potentiation of habenular AMPAR transmission mimics and rescues stress-driven cognitive deficits

(A) Experimental timeline. Representative injection site of AAV-hM3Dq (scale bar: 100 μm).

(B) Example traces of AMPA/NMDA (scale bars: 30 pA and 10 ms). Boxplots and scatterplots of AMPA/NMDA from control/GFP mice (black: n = 3 mice/13 cells, 2.353 ± 0.4565), stress/GFP mice (red: n = 3 mice/11 cells, 0.4818 ± 0.1509), and control/M3Dq mice (blue: n = 3 mice/12 cells, 0.5575 ± 0.1453). One-way ANOVA ($F_{2,33}$ = 12.18) with Holm-Sidak correction (***p < 0.001, comparisons against control/GFP).

(C) Experimental timeline. Boxplots and scatterplots of the error incidence in control/GFP mice (black: n = 12 mice, 6.833 ± 1.043 during habituation and 4.167 ± 0.6134 during test), stress/GFP mice (red: n = 12 mice, 5.75 ± 0.7295 during habituation and 8.75 ± 1.262 during test), and control/M3Dq mice (blue: n = 15 mice, 5.533 ± 0.5152 during habituation and 8 ± 0.8338 during test). Two-way repeated-measure ANOVA ($F_{1,36}$ = 2.342) with Sidak correction (*p < 0.05, habituation versus test).

(D) Representative injection site of AAV-Rab5 (scale bar: 100 μm). Experimental timeline.

(E) Example traces of AMPA/NMDA (scale bars: 25 pA and 10 ms). Boxplots and scatterplots of AMPA/NMDA (GFP, black: n = 3 mice/15 cells, 2.391 ± 0.4619; Rab5, red: n = 5 mice/20 cells, 0.938 ± 0.116). Mann-Whitney test (U = 74.5, *p < 0.05).

(legend continued on next page)

adaptation by capitalizing on the concept of homeostatic downscaling, whereby prolonged neuronal hyperactivity reduces the strength of synaptic transmission (Pan-Vazquez et al., 2020; Pati et al., 2019; Turrigiano, 2008). We injected an hM3Dq-encoding AAV (rAAV$_{8.2}$-hSyn1-hM3Dq-mCherry) into the LHb, allowing neuronal depolarization after exposure to the specific ligand clozapine N-oxide (CNO) (Figures S4A and S4B). Repeated intraperitoneal CNO administration, throughout one day or six consecutive days, decreased AMPA/NMDA and the amplitude of miniature EPSCs 12 h after the last CNO exposure, reproducing the stress-driven synaptic depression (Figures 4A, 4B, and S4C). Consequently, two daily CNO administrations in the intervening days between habituation and test session increased the number of errors at day 8 of the T-maze task (Figure 4C). Hence, LHb-specific weakening of excitatory synapses is sufficient to recapitulate stress-driven maladaptations in reward-guided performance.

However, homeostatic downscaling remains an indirect intervention to reduce excitatory synaptic transmission. Rab5 and Rac1 are small guanosine triphosphatases (GTPases) that weaken and potentiate AMPAR expression and function, respectively (Brown et al., 2005; Wright et al., 2020). Viral Rab5 overexpression within the LHb (rAAV$_{8.2}$-hSyn1-eGFP-Rab5) reduced AMPA/NMDA and increased the number of errors during the reward-guided task, simulating stress-driven synaptic adaptation and subsequent behavioral impairment (Figures 4D–4F and S4A). A drawback of this manipulation is the weak temporal control of Rab5 overexpression, because the reduction in AMPAR transmission occurs before the behavioral assessment. To overcome this limitation, we virally delivered a photoactivatable (PA) version of Rac1 in the LHb (rAAV$_{8.2}$-hSyn1-eGFP-PA-Rac1), which enables the potentiation of AMPAR transmission to be spatially and temporally restricted (Wright et al., 2020). Blue light exposure (473 nm) potentiated AMPAR currents onto LHb neurons in acute brain slices (Figure S4D). We then transduced PA-Rac1 in the LHb and concomitantly implanted an optic fiber above the site of injection (Figures 4G, S4A, and S4E). Animals underwent habituation and were (or not) exposed to stimulation with blue light at day 8, immediately before the test session (1 Hz, 40 minutes). Stress-exposed mice subjected to blue light performed a similar number of errors as the control group, in contrast with their stressed counterparts not exposed to blue light (Figures 4H and S4F). We then recorded *ex vivo* AMPA/NMDA from a cohort of these mice. Although PA-Rac1 overexpression in the absence of light left unaltered the stress-driven reduction in AMPA/NMDA, *in vivo* Rac1 photoactivation normalized this parameter (Figure 4I). Interestingly, the resulting AMPA/NMDA values fell within a linear regression comparable with that of the naive mice in Figure 1J (Figures 4I and S4G). These data reinforce a scenario in which the strength of excitatory synapses in LHb neurons predicts the error incidence during the test session of the reward-guided task.

DISCUSSION

The LHb represents a core neuronal substrate for aversive behaviors, depressive symptoms, and coping strategies (Hu et al., 2020). Furthermore, stress biases the LHb encoding of positive and negative stimuli, likely contributing to pathological states (Shabel et al., 2019). We highlight here an unconventional facet of LHb neurons by providing a synaptic foundation governing cognitive performance during appetitive behaviors.

A synaptic framework for cognitive performance

Despite the central role of cognitive computations during reward-guided choices, their neuronal underpinnings are a matter of debate. Within the mammalian brain, decisions are made not by single neuronal domains but by the collective dynamics of multiple brain circuits (Wang, 2008). Animal physiology and human functional imaging defined the activity and synaptic strength in the prefrontal cortex as instrumental contributors to the control of decision-making (Arnsten et al., 2012). In our study, we propose that excitatory synaptic transmission within a subcortical node is required for reward-guided cognitive performance. Namely, we show that the low strength of AMPAR transmission in LHb neurons predicts a high incidence of errors during reward pursuit. Stress-driven synaptic depression, as well as LHb optical silencing, drives cognitive deficits through the disruption of reward omission encoding. Our photometric analysis highlights that such a process emerges during the test session, coinciding with the time in which the association between context and reward is already in place (Cherng et al., 2020; Palumbo et al., 2020). Future studies will need to elucidate whether LHb synaptic strength and neuronal activity are universal for shaping the performance during cognitive processes of an alternative nature. This is a plausible scenario, because pharmacological blockade of habenular glutamate receptors compromises the retrieval of spatial memories (Mathis et al., 2015). NMDAR decrease and dendritic spine loss in the prefrontal cortex contribute to working-memory deficits (Arnsten et al., 2012; Hains et al., 2009). In the hippocampus, AMPAR reduction mediates the emergence of adaptive behaviors in spatial memory

(F) Boxplots and scatterplots of the error incidence (GFP, black: n = 13 mice, 6.538 ± 0.9715 during habituation and 5.231 ± 0.9881 during test; Rab5, red: n = 14 mice, 10.79 ± 1.1 during habituation and 10.43 ± 1.848 during test). Two-way repeated-measure ANOVA ($F_{1,25}$ = 9.965, **p < 0.01, GFP versus Rab5 interaction).
(G) Representative injection site of AAV-PA-Rac1 and fiber implantation (scale bar: 200 μm).
(H) Experimental timeline. Boxplots and scatterplots of the error incidence in PA-Rac1 mice subjected to control/light (black: n = 11 mice, 6.636 ± 1.591 during habituation and 4.545 ± 1.729 during test), stress/no-light (red: n = 14 mice, 4.429 ± 0.9061 during habituation and 10.36 ± 1.393 during test), and stress/light (blue: n = 15 mice, 5.933 ± 0.8421 during habituation and 5 ± 1.317 during test). Two-way repeated-measure ANOVA ($F_{1,37}$ = 0.9971) with Sidak correction (**p < 0.01, habituation versus test).
(I) Example traces of AMPA/NMDA (scale bars: 20 pA and 5 ms). Boxplots and scatterplots of AMPA/NMDA from a cohort of mice in (H) (black: control/light, n = 2 mice/10 cells, 2.454 ± 0.466; red: stress/no-light, n = 3 mice/11 cells, 0.8827 ± 0.1408; blue: stress/light, n = 3 mice/14 cells, 1.726 ± 0.2739). One-way ANOVA ($F_{2,32}$ = 5.882, **p < 0.01). Overlay of the stressed PA-Rac1 mice onto the correlation analysis of Figure 1J (open circles: individual values; closed circles: single-mouse averages; n = 6 mice/25 cells).
Data are represented with boxplots (median and quartiles) or mean ± SEM. See also Figure S4.

tasks (Awasthi et al., 2019). Therefore, synaptic depression of excitatory transmission throughout the brain may represent a common substrate to modulate diverse cognitive functions.

Mechanistic and circuit understanding of stress-driven cognitive deficits

Stressful life events constitute a key environmental risk factor for the development of neuropsychiatric disorders (Monroe and Harkness, 2005). In addition, stress exerts aberrant effects on the structure and function of excitatory synapses in multiple brain regions (Thompson et al., 2015). Both acute and chronic stressors perturb LHb function, yet this occurs through distinct mechanisms and by engaging diverse neuronal circuits (Cerniauskas et al., 2019; Knowland et al., 2017; Lecca et al., 2016; Li et al., 2011; Shabel et al., 2014). Our observation that a stressful experience drives AMPAR synaptic depression in LHb neurons supports the general framework whereby aberrant synaptic transmission underlies stress-driven behavioral deficits. However, specific examination of the NMDAR component after stress is necessary to understand the complete landscape of cellular adaptations at excitatory synapses. Notably, the induction mechanism of habenular AMPAR downscaling remains unknown. In zebrafish, prolonged stress engages the progressive recruitment of larger neuronal ensembles (Andalman et al., 2019). AMPAR two-photon monitoring at individual spines opens an opportunity to test whether stress-driven synaptic depression originates at discrete LHb neurons and synapses and subsequently spreads to neighboring ones (Roth et al., 2020).

The AMPAR depression described here lacks input specificity, thereby contrasting with the prevailing view that behavioral adaptations often rely on plasticity within precise neuronal circuits (LeGates et al., 2018; Pascoli et al., 2018; Zhou et al., 2019). However, our data do not rule out output circuit specificity. Accordingly, LHb innervation of neurons in the rostromedial tegmental nucleus mediates reward prediction error responses, positioning the LHb-to-midbrain projection as a novel element for cognitive performance (Li et al., 2019). The diverse LHb neuronal clusters emerging based on molecular diversity, as well as anatomical projection targets, might prove useful in defining whether stress-driven modifications follow a clear biological rule (Hashikawa et al., 2020; Wallace et al., 2020).

Altogether, the present work unravels the instrumental role of excitatory transmission within a subcortical node essential to avoid reward omissions, a fundamental module governing appetitive behaviors.

STAR★METHODS

Detailed methods are provided in the online version of this paper and include the following:

- KEY RESOURCES TABLE
- RESOURCE AVAILABILITY
  - Lead contact
  - Materials availability
  - Data and code availability
- EXPERIMENTAL MODEL AND SUBJECT DETAILS
- METHOD DETAILS
  - Stereotaxic surgeries
  - Stress paradigms
  - T-maze paradigm
  - Fiber photometry
  - Viral manipulations
  - Electrophysiology in acute brain slices
  - Glutamate uncaging
  - Single-unit recordings under anesthesia
  - Histology
  - Array tomography
- QUANTIFICATION AND STATISTICAL ANALYSIS

SUPPLEMENTAL INFORMATION

Supplemental Information can be found online at https://doi.org/10.1016/j.neuron.2021.01.008.

ACKNOWLEDGMENTS

We thank the Mameli laboratory, F.J. Meye, D. Jabaudon, J.A. Esteban, and C. Lüscher for their feedback on the manuscript. We thank the UZH Viral Vector Facility for technical support. We thank J.A. Esteban (CSIC, Madrid) for providing the Rab5 construct. This work was supported by a European Starting Grant (ERC SalienSy 335333), Swiss National Funding (31003A) to M.M., NCCR Synapsy (51NF40-158776), and Swiss National Funding (310030-182651/1) to C.B.

AUTHOR CONTRIBUTIONS

A.N.-P. performed and analyzed electrophysiological recordings and behavioral experiments. M.T., A.L.L., M.C., A.T., and M.M. helped with electrophysiology and behavior. S.L. assisted with photometric recordings. M.S.-R. performed and analyzed array tomography experiments. D.G. and C.B. conducted and analyzed biochemical studies. M.M. and A.N.-P. designed the study and wrote the manuscript with the help of all authors.

DECLARATION OF INTERESTS

The authors declare no competing interests.

Received: April 24, 2020
Revised: October 5, 2020
Accepted: January 8, 2021
Published: February 2, 2021

REFERENCES

Andalman, A.S., Burns, V.M., Lovett-Barron, M., Broxton, M., Poole, B., Yang, S.J., Grosenick, L., Lerner, T.N., Chen, R., Benster, T., et al. (2019). Neuronal Dynamics Regulating Brain and Behavioral State Transitions. Cell *177*, 970–985.e20.

Arnsten, A.F. (2015). Stress weakens prefrontal networks: molecular insults to higher cognition. Nat. Neurosci. *18*, 1376–1385.

Arnsten, A.F., Wang, M.J., and Paspalas, C.D. (2012). Neuromodulation of thought: flexibilities and vulnerabilities in prefrontal cortical network synapses. Neuron *76*, 223–239.

Awasthi, A., Ramachandran, B., Ahmed, S., Benito, E., Shinoda, Y., Nitzan, N., Heukamp, A., Rannio, S., Martens, H., Barth, J., et al. (2019). Synaptotagmin-3 drives AMPA receptor endocytosis, depression of synapse strength, and forgetting. Science *363*, 6422.

Baker, P.M., Oh, S.E., Kidder, K.S., and Mizumori, S.J. (2015). Ongoing behavioral state information signaled in the lateral habenula guides choice flexibility in freely moving rats. Front. Behav. Neurosci. *9*, 295.

Baker, P.M., Raynor, S.A., Francis, N.T., and Mizumori, S.J. (2017). Lateral habenula integration of proactive and retroactive information mediates behavioral flexibility. Neuroscience *345*, 89–98.

Brown, T.C., Tran, I.C., Backos, D.S., and Esteban, J.A. (2005). NMDA receptor-dependent activation of the small GTPase Rab5 drives the removal of synaptic AMPA receptors during hippocampal LTD. Neuron *45*, 81–94.

Cerniauskas, I., Winterer, J., de Jong, J.W., Lukacsovich, D., Yang, H., Khan, F., Peck, J.R., Obayashi, S.K., Lilascharoen, V., Lim, B.K., et al. (2019). Chronic Stress Induces Activity, Synaptic, and Transcriptional Remodeling of the Lateral Habenula Associated with Deficits in Motivated Behaviors. Neuron *104*, 899–915.e8.

Cherng, B.W., Islam, T., Torigoe, M., Tsuboi, T., and Okamoto, H. (2020). The Dorsal Lateral Habenula-Interpeduncular Nucleus Pathway Is Essential for Left-Right-Dependent Decision Making in Zebrafish. Cell Rep. *32*, 108143.

Chuong, A.S., Miri, M.L., Busskamp, V., Matthews, G.A., Acker, L.C., Sørensen, A.T., Young, A., Klapoetke, N.C., Henninger, M.A., Kodandaramaiah, S.B., et al. (2014). Noninvasive optical inhibition with a red-shifted microbial rhodopsin. Nat Neurosci *17*, 1123–1129.

Cui, G., Jun, S.B., Jin, X., Luo, G., Pham, M.D., Lovinger, D.M., Vogel, S.S., and Costa, R.M. (2014). Deep brain optical measurements of cell type-specific neural activity in behaving mice. Nat. Protoc. *9*, 1213–1228.

Cui, Y., Yang, Y., Ni, Z., Dong, Y., Cai, G., Foncelle, A., Ma, S., Sang, K., Tang, S., Li, Y., et al. (2018). Astroglial Kir4.1 in the lateral habenula drives neuronal bursts in depression. Nature *554*, 323–327.

Friedman, A., Homma, D., Bloem, B., Gibb, L.G., Amemori, K.I., Hu, D., Delcasso, S., Truong, T.F., Yang, J., Hood, A.S., et al. (2017). Chronic Stress Alters Striosome-Circuit Dynamics, Leading to Aberrant Decision-Making. Cell *171*, 1191–1205.e28.

Hains, A.B., Vu, M.A., Maciejewski, P.K., van Dyck, C.H., Gottron, M., and Arnsten, A.F. (2009). Inhibition of protein kinase C signaling protects prefrontal cortex dendritic spines and cognition from the effects of chronic stress. Proc. Natl. Acad. Sci. USA *106*, 17957–17962.

Halassa, M.M., and Kastner, S. (2017). Thalamic functions in distributed cognitive control. Nat. Neurosci. *20*, 1669–1679.

Hashikawa, Y., Hashikawa, K., Rossi, M.A., Basiri, M.L., Liu, Y., Johnston, N.L., Ahmad, O.R., and Stuber, G.D. (2020). Transcriptional and Spatial Resolution of Cell Types in the Mammalian Habenula. Neuron *106*, 743–758.e5.

Hu, H., Cui, Y., and Yang, Y. (2020). Circuits and functions of the lateral habenula in health and in disease. Nat. Rev. Neurosci. *21*, 277–295.

Knowland, D., Lilascharoen, V., Pacia, C.P., Shin, S., Wang, E.H., and Lim, B.K. (2017). Distinct Ventral Pallidal Neural Populations Mediate Separate Symptoms of Depression. Cell *170*, 284–297.e18.

Lazaridis, I., Tzortzi, O., Weglage, M., Märtin, A., Xuan, Y., Parent, M., Johansson, Y., Fuzik, J., Fürth, D., Fenno, L.E., et al. (2019). A hypothalamus-habenula circuit controls aversion. Mol. Psychiatry *24*, 1351–1368.

Lecca, S., Meye, F.J., and Mameli, M. (2014). The lateral habenula in addiction and depression: an anatomical, synaptic and behavioral overview. Eur. J. Neurosci. *39*, 1170–1178.

Lecca, S., Pelosi, A., Tchenio, A., Moutkine, I., Lujan, R., Hervé, D., and Mameli, M. (2016). Rescue of GABAB and GIRK function in the lateral habenula by protein phosphatase 2A inhibition ameliorates depression-like phenotypes in mice. Nat. Med. *22*, 254–261.

Lecourtier, L., Neijt, H.C., and Kelly, P.H. (2004). Habenula lesions cause impaired cognitive performance in rats: implications for schizophrenia. Eur. J. Neurosci. *19*, 2551–2560.

LeGates, T.A., Kvarta, M.D., Tooley, J.R., Francis, T.C., Lobo, M.K., Creed, M.C., and Thompson, S.M. (2018). Reward behaviour is regulated by the strength of hippocampus-nucleus accumbens synapses. Nature *564*, 258–262.

Li, B., Piriz, J., Mirrione, M., Chung, C., Proulx, C.D., Schulz, D., Henn, F., and Malinow, R. (2011). Synaptic potentiation onto habenula neurons in the learned helplessness model of depression. Nature *470*, 535–539.

Li, H., Vento, P.J., Parrilla-Carrero, J., Pullmann, D., Chao, Y.S., Eid, M., and Jhou, T.C. (2019). Three Rostromedial Tegmental Afferents Drive Triply Dissociable Aspects of Punishment Learning and Aversive Valence Encoding. Neuron *104*, 987–999.e4.

Lüthi, A., and Lüscher, C. (2014). Pathological circuit function underlying addiction and anxiety disorders. Nat. Neurosci. *17*, 1635–1643.

Mathis, V., Cosquer, B., Avallone, M., Cassel, J.C., and Lecourtier, L. (2015). Excitatory Transmission to the Lateral Habenula Is Critical for Encoding and Retrieval of Spatial Memory. Neuropsychopharmacology *40*, 2843–2851.

Matsumoto, M., and Hikosaka, O. (2007). Lateral habenula as a source of negative reward signals in dopamine neurons. Nature *447*, 1111–1115.

Monroe, S.M., and Harkness, K.L. (2005). Life stress, the "kindling" hypothesis, and the recurrence of depression: considerations from a life stress perspective. Psychol. Rev. *112*, 417–445.

Nielson, H.C., and McIver, A.H. (1966). Cold stress and habenular lesion effects on rat behaviors. J. Appl. Physiol. *21*, 655–660.

Palumbo, F., Serneels, B., Pelgrims, R., and Yaksi, E. (2020). The Zebrafish Dorsolateral Habenula Is Required for Updating Learned Behaviors. Cell Rep. *32*, 108054.

Pan-Vazquez, A., Wefelmeyer, W., Gonzalez Sabater, V., Neves, G., and Burrone, J. (2020). Activity-Dependent Plasticity of Axo-axonic Synapses at the Axon Initial Segment. Neuron *106*, 265–276.e6.

Pascoli, V., Hiver, A., Van Zessen, R., Loureiro, M., Achargui, R., Harada, M., Flakowski, J., and Lüscher, C. (2018). Stochastic synaptic plasticity underlying compulsion in a model of addiction. Nature *564*, 366–371.

Pati, S., Salvi, S.S., Kallianpur, M., Vaidya, B., Banerjee, A., Maiti, S., Clement, J.P., and Vaidya, V.A. (2019). Chemogenetic Activation of Excitatory Neurons Alters Hippocampal Neurotransmission in a Dose-Dependent Manner. eNeuro *6*, ENEURO.0124-19.2019.

Root, D.H., Mejias-Aponte, C.A., Zhang, S., Wang, H.L., Hoffman, A.F., Lupica, C.R., and Morales, M. (2014). Single rodent mesohabenular axons release glutamate and GABA. Nat. Neurosci. *17*, 1543–1551.

Roth, R.H., Cudmore, R.H., Tan, H.L., Hong, I., Zhang, Y., and Huganir, R.L. (2020). Cortical Synaptic AMPA Receptor Plasticity during Motor Learning. Neuron *105*, 895–908.e5.

Schwabe, L., and Wolf, O.T. (2009). The context counts: congruent learning and testing environments prevent memory retrieval impairment following stress. Cogn. Affect. Behav. Neurosci. *9*, 229–236.

Shabel, S.J., Proulx, C.D., Trias, A., Murphy, R.T., and Malinow, R. (2012). Input to the lateral habenula from the basal ganglia is excitatory, aversive, and suppressed by serotonin. Neuron *74*, 475–481.

Shabel, S.J., Proulx, C.D., Piriz, J., and Malinow, R. (2014). Mood regulation. GABA/glutamate co-release controls habenula output and is modified by antidepressant treatment. Science *345*, 1494–1498.

Shabel, S.J., Wang, C., Monk, B., Aronson, S., and Malinow, R. (2019). Stress transforms lateral habenula reward responses into punishment signals. Proc. Natl. Acad. Sci. USA *116*, 12488–12493.

Sousa, N., and Almeida, O.F. (2012). Disconnection and reconnection: the morphological basis of (mal)adaptation to stress. Trends Neurosci. *35*, 742–751.

Stamatakis, A.M., and Stuber, G.D. (2012). Activation of lateral habenula inputs to the ventral midbrain promotes behavioral avoidance. Nat. Neurosci. *15*, 1105–1107.

Stamatakis, A.M., Van Swieten, M., Basiri, M.L., Blair, G.A., Kantak, P., and Stuber, G.D. (2016). Lateral Hypothalamic Area Glutamatergic Neurons and Their Projections to the Lateral Habenula Regulate Feeding and Reward. J. Neurosci. *36*, 302–311.

Stopper, C.M., and Floresco, S.B. (2014). What's better for me? Fundamental role for lateral habenula in promoting subjective decision biases. Nat. Neurosci. *17*, 33–35.

Thompson, S.M., Kallarackal, A.J., Kvarta, M.D., Van Dyke, A.M., LeGates, T.A., and Cai, X. (2015). An excitatory synapse hypothesis of depression. Trends Neurosci. *38*, 279–294.

Thornton, E.W., and Evans, J.A. (1984). The effects of lesions of the habenula nucleus on lever press behaviour during a tandem operant schedule with contrasting response requirements. Behav. Brain Res. *12*, 327–334.

Trusel, M., Nuno-Perez, A., Lecca, S., Harada, H., Lalive, A.L., Congiu, M., Takemoto, K., Takahashi, T., Ferraguti, F., and Mameli, M. (2019). Punishment-Predictive Cues Guide Avoidance through Potentiation of Hypothalamus-to-Habenula Synapses. Neuron *102*, 120–127.e4.

Turrigiano, G.G. (2008). The self-tuning neuron: synaptic scaling of excitatory synapses. Cell *135*, 422–435.

Wallace, M.L., Huang, K.W., Hochbaum, D., Hyun, M., Radeljic, G., and Sabatini, B.L. (2020). Anatomical and single-cell transcriptional profiling of the murine habenular complex. eLife *9*, e51271.

Wang, X.J. (2008). Decision making in recurrent neuronal circuits. Neuron *60*, 215–234.

Wright, W.J., Graziane, N.M., Neumann, P.A., Hamilton, P.J., Cates, H.M., Fuerst, L., Spenceley, A., MacKinnon-Booth, N., Iyer, K., Huang, Y.H., et al. (2020). Silent synapses dictate cocaine memory destabilization and reconsolidation. Nat. Neurosci. *23*, 32–46.

Zhou, W., Jin, Y., Meng, Q., Zhu, X., Bai, T., Tian, Y., Mao, Y., Wang, L., Xie, W., Zhong, H., et al. (2019). A neural circuit for comorbid depressive symptoms in chronic pain. Nat. Neurosci. *22*, 1649–1658.

STAR★METHODS

KEY RESOURCES TABLE

REAGENT or RESOURCE	SOURCE	IDENTIFIER
Antibodies		
Anti-Synapsin-1 (rabbit)	Cell Signaling Technology	AB_2616578
Anti-GluA1 (mouse)	Millipore	AB_11212678
Anti-GluN1 (mouse)	Millipore	AB_94946
Donkey anti-rabbit Alexa Fluor 647	Jackson ImmunoResearch	AB_2492288
Donkey anti-mouse Alexa Fluor 488	Jackson ImmunoResearch	AB_2340846
Donkey anti-mouse Cy3	Jackson ImmunoResearch	AB_2340813
Virus strains		
$rAAV_{2.5}$-hSyn1-CoChR-eGFP	UNC Vector Core	N/A
$rAAV_{1/2}$-hSyn1-$ChR2_{H134R}$-eGFP	UZH Vector Facility	v221-1
$rAAV_{2.5}$-hSyn1-GCaMP6f	Gift from G. Keller (FMI, Basel)	N/A
$rAAV_{8}$-hSyn1-JAWS-GFP	Chuong et al., 2014	Addgene_65014
$rAAV_{8.2}$-hSyn1-hM3Dq-mCherry	UZH Vector Facility	v101-8
$rAAV_{8.2}$-hSyn1-eGFP-Rab5	UZH Vector Facility	v435-8
$rAAV_{8.2}$-hSyn1-eGFP-PA-Rac1	UZH Vector Facility	v371-8
$rAAV_{8.2}$-hSyn1-eGFP	UZH Vector Facility	v81-8
Chemicals, peptides, and recombinant proteins		
Picrotoxin	Hello Bio	HB0506
APV	Hello Bio	HB0225
NBQX disodium salt	Hello Bio	HB0443
MNI-caged L-glutamate	Hello Bio	HB0423
Tetrodotoxin citrate	Hello Bio	HB1035
NASPM trihydrochloride	Hello Bio	HB0441
Clozapine N-oxide dihydrochloride	Hello Bio	HB6149

RESOURCE AVAILABILITY

Lead contact

Further information and requests for resources and reagents should be directed to and will be fulfilled by the Lead Contact, Manuel Mameli (manuel.mameli@unil.ch).

Materials availability

This study did not generate new unique reagents.

Data and code availability

Original data for all figures and datasets in this paper are available upon request to the lead contact. This study did not generate new code.

EXPERIMENTAL MODEL AND SUBJECT DETAILS

Male mice were purchased from Janvier (C57BL6/J) and housed in groups of three-to-five per cage (4-12 weeks old). Food and water were provided *ad libitum* unless otherwise specified, and light-dark phases lasted 12 hours (from 7 a.m. to 7 p.m.). All procedures aimed to fulfil the 3R criterion (i.e., replacement, reduction and refinement) and were approved by the veterinary offices of Vaud (Switzerland; license VD3171).

METHOD DETAILS

Stereotaxic surgeries

4-6 week-old mice were anesthetized with ketamine (150 mg/kg) and xylazine (100 mg/kg) before bilateral injection of $rAAV_{2.5}$-hSyn1-CoChR-eGFP (titer = $1x10^{12}$ vg/mL) or $rAAV_{1/2}$-hSyn1-$ChR2_{H134R}$-eGFP (titer = $3.3x10^{13}$ vg/mL) in the lateral hypothalamus (AP −1.25 from bregma; ML ± 1.0; DV −5.1), entopeduncular nucleus (AP −1.2 from bregma; ML ± 1.8; DV −4.5), bed nucleus of the stria terminalis (AP +0.3 from bregma; ML ± 0.9; DV −4.55) or medial ventral tegmental area (AP −2 from bregma; ML ± 0.25; DV −4.6). Optogenetic recordings in acute brains slices were performed 3-4 weeks after stereotactic viral injection. $rAAV_{2.5}$-hSyn1-GCaMP6f (titer = $5x10^{12}$ vg/mL, 1:5 dilution), $rAAV_8$-hSyn1-JAWS-GFP (titer = $1.3x10^{13}$ vg/mL), $rAAV_{8.2}$-hSyn1-hM3Dq-mCherry (titer = $5.4x10^{12}$ vg/mL), $rAAV_{8.2}$-hSyn1-eGFP-Rab5 (titer = $6.4x10^{12}$ vg/mL), $rAAV_{8.2}$-hSyn1-eGFP-PA-Rac1 (titer = $1.2x10^{12}$ vg/mL) or $rAAV_{8.2}$-hSyn1-eGFP (titer = $9.4x10^{12}$ vg/mL) were injected in the LHb (AP −1.32 from bregma; ML ± 0.42; DV −2.8). Viral serotypes were chosen considering the level of expression and cell viability assessed in previous studies (Trusel et al., 2019). Optic fibers were concomitantly implanted for photometric experiments (Chi Square Bioimaging; DV −2.65), photoactivation of PA-Rac1 (Thorlabs; DV −2.3) and JAWS-driven optical silencing of LHb neurons (Thorlabs; DV −2.3). Mice were exposed to the T-maze task 3-4 weeks after surgery (7-10 week-old). Injection sites and fiber placements were checked for each animal, and mice with incorrect targeting were discarded from the analysis.

Stress paradigms

Foot-shock exposure

7-12 week-old mice were introduced in an operant conditioning chamber with a metal grid on the ground (Ugo Basile). Mice were subjected to a 20-minute session during which they received either 19 (stress) or 0 (control) unpredictable foot shocks with a randomized inter-shock interval of 1-90 s (1 mA intensity, 500 ms duration). Unless otherwise specified, mice were anesthetized for patch-clamp electrophysiology 24 hours after stress exposure. Alternatively, mice were exposed to the foot-shock paradigm 1 day after the habituation session and 6 days before the test session of the T-maze task.

Acute restraint stress

7-12 week-old mice were introduced inside a polyethylene tube (Falcon, 50 mL) during 1.5 hours. For control mice, the tube was introduced in their home cage. Recordings were performed 24 hours after the end of the session.

T-maze paradigm

The T-maze apparatus consisted of a central arm and two side arms (Ugo Basile). The maze was placed 65 cm above the floor. Arm dimensions were 5 cm width, 12 cm height and 35 cm length. One of the arms was systematically baited with a food reward (regular chow, 10 mg) while the opposite arm remained neutral (i.e., absence of reward). Mice were first exposed to the T-maze during the habituation session (day 1), and re-exposed one week later during the test session (day 8). During the latter, unless otherwise stated, arm outcomes were inverted. 48 hours before each session, mice were moved from their home cages to a new cage without food but with water *ad libitum*. Mice were habituated to the T-maze room for at least 1 hour before the commencement of each session. During the habituation and test session, 7-12 week-old mice were placed in the central arm at the beginning of every trial and subsequently chose between the two alternative side arms. When the whole body of the mouse was inside the chosen arm, the door was closed with a remote electronic system. Once the animal consumed the food reward or explored the non-rewarded container, the experimenter brought back the mouse to the home cage and baited, if needed, the rewarded arm with a fresh food pellet. Unless otherwise specified, both sessions were stopped whenever mice would choose the rewarded arm for 5 consecutive times, or after 35 trials provided the completion criterion was not reached. For photometric experiments, with analytical and statistical purposes, the number of errors and rewarded turns was increased by exposing mice to 50 trials in each session. Early and late error trials were categorized as those occurring within the first (0%–25%) and last quarter (75%–100%) during the test session, respectively. All sessions were recorded under infrared light (Noldus). For the calculation of the time needed to reach the container located at the end of the arms, the first 5 trials of the habituation and test session were used for each mouse. Transition probabilities were calculated on a single-mouse basis with the following formula, where $n_{i\rightarrow j}$ denotes the number of transitions between states (i.e., reward or error) and N represents the total amount of transitions:

$$P_{i\rightarrow j} = \frac{n_{i\rightarrow j}}{N} \Big/ \Big/ \sum P_{i\rightarrow j} = 1.$$

Fiber photometry

Experiments were performed with the χ^2-200 system (Chi Square Bioimaging). Blue light from a picosecond-pulsed laser was delivered to the LHb through a single-mode fiber (473 nm, 50 MHz, 80 picosecond full width at half maximum), whereas fluorescence emission was collected from the tissue with a multi-mode fiber. Both fibers were cannulated together throughout a cable, at the end of which a detachable ferrule was connected to the fiber implant located inside the mouse brain. FF01-550/88 bandpass filter was applied over the emitted photons collected by the multi-mode fiber (Semrock). Photons were recorded using a module of time-correlated single-photon counting SPC-130-EMN (Becker & Hickl GmbH). For consistency, calcium signals from all mice included in the present study were acquired using the same gain.

Viral manipulations

For the JAWS optical silencing (mice injected with rAAV$_8$-hSyn1-JAWS-GFP), red light (638 nm, 8 mW, continuous light) was shined during the test session aligned to the entry into the non-rewarded container, using a laser (MatchBox Integrated Optics) coupled to a Master-8 (AMPI) through a TTL system. Regarding the chemogenetic AMPAR downscaling *ex vivo* (mice injected with rAAV$_{8.2}$-hSyn1-hM3Dq-mCherry), three injections of clozapine N-oxide (CNO, 1 mg/kg) were administered intraperitoneally with a time separation of ±6 hours and, 12 hours after the last CNO injection, AMPA/NMDA recordings were performed (7-10 week-old mice). The timeline for these *ex vivo* recordings was chosen to examine the rapid repercussions of LHb hyperactivity driven by hM3Dq on excitatory transmission. For behavioral experiments, CNO was administered intraperitoneally twice per day (1 mg/kg) with a time separation of ±6 hours, during the intervening days between habituation and test session of the T-maze paradigm. In order to probe AMPAR transmission, the same timeline was used for *ex vivo* miniature EPSC recordings. For the photoactivation of PA-Rac1 (mice injected with rAAV$_{8.2}$-hSyn1-eGFP-PA-Rac1), mice were exposed to blue-light stimulation immediately prior to the test session (473 nm, 6-9 mW, 1 Hz, 150 ms pulses for 40 minutes), using a laser (Shanghai Dream Lasers Technology) coupled to a Master-8 (AMPI) through a TTL system. The same optical protocol was employed in acute brain slices to monitor AMPAR current amplitudes.

Electrophysiology in acute brain slices

7-12 week-old mice were anaesthetized with ketamine (150 mg/kg) and xylazine (100 mg/kg) prior to slice preparation. Coronal brain slices (thickness: 250 μm) containing the LHb were cut while immersed in ice-cold solution, bubbled with 95% O_2 and 5% CO_2 and containing the following reagents (in mM): Choline chloride (110); glucose (25); $NaHCO_3$ (25); $MgCl_2$ (7); ascorbic acid (11.6); sodium pyruvate (3.1); KCl (2.5); NaH_2PO_4 (1.25); and $CaCl_2$ (0.5). Slices were then allowed to recover for 1 hour at room temperature in artificial cerebrospinal fluid (ACSF) containing the following reagents (in mM): NaCl (124); $NaHCO_3$ (26.2); glucose (11); KCl (2.5); $CaCl_2$ (2.5); $MgCl_2$ (1.3); and NaH_2PO_4 (1). Borosilicate glass pipettes (Phymep; impedance: 2.5-4 MΩ) were filled with CsCl-based intracellular solution containing the following reagents (in mM): CsCl (130); NaCl (4); creatine phosphate (5); $MgCl_2$ (2); Na_2ATP (2); Na_3GTP (0.6); EGTA (1.1); HEPES (5); and spermine (0.1). Whole-cell voltage-clamp recordings were obtained from LHb neurons at 34°C with a perfusion flow rate of 2.5 mL/min. Throughout the recordings, electrical signal was filtered (5 kHz) and digitized (10 kHz) using MultiClamp 200B (Molecular Devices). Data acquisition was performed with Igor Pro and NIDAQ tools (Wave Metrics). Access resistance was continuously monitored with a voltage step of −4 mV (0.1 Hz). In electrical stimulation experiments, the electrode was introduced inside a glass pipette filled with ACSF and placed within the LHb to evoke EPSCs through an ISO-Flex stimulator coupled to a Master-8 (AMPI). For optogenetic experiments, EPSCs were evoked with an LED coupled to an Olympus-BX51 microscope delivering pulses of blue light (Cool LED; 473 nm, 5 mW, 1-10 ms duration). AMPAR currents, for the measurement of AMPA/NMDA (+40 mV), were pharmacologically isolated by bath application of picrotoxin (PTX, $GABA_AR$ antagonist; 100 μM) and D-2-amino-5-phosphonopentanoic acid (APV, NMDAR antagonist; 100 μM). NMDAR currents were calculated by subtraction analysis. AMPA/NMDA assessment was performed 1-4 days after T-maze in order to maximize the yield of recordings from the same cohort of animals employed for the behavioral experiments. AMPAR miniature EPSCs (−60 mV) were pharmacologically isolated with PTX and APV under bath application of tetrodotoxin (TTX, sodium channel blocker; 1 μM). NMDAR spontaneous EPSCs (−60 mV) were pharmacologically isolated with PTX and NBQX (AMPAR antagonist; 10 μM) in Mg^{2+}-free ACSF. EPSC trains were obtained at a frequency of 20 Hz in the presence of PTX and APV (−50 mV for electrical stimulation, −60 mV for input-specific). Timelines of AMPAR currents were recorded at −50 mV for NASPM-sensitivity experiments (30 μM) and at −60 mV for the photoactivation of PA-Rac1 (473 nm light, 1 Hz, 150 ms pulses), in the presence of PTX and APV. Whole-cell current-clamp recordings were performed to examine the CNO-induced depolarization (10 μM) in the presence of PTX, APV and NBQX. AMPAR rectification index (RI) was calculated under bath application of PTX and APV with the following formula, where I denotes current amplitude in pA:

$$RI = \frac{(-I_{-60}/I_{+40})}{(60/40)}$$

Glutamate uncaging

For MNI-glutamate uncaging (4-methoxy-7-nitroindolinyl-caged L-glutamate; 200 μM, Tocris), a single-path photolysis head was connected to a solid-state laser (Rapp OptoElectronic; 405 nm, 0.5 ms duration of optical pulse, 3-5 μm diameter of photolysis beam). Alignment of the laser path at the center of the recording chambers allowed localization of the photolysis area within the sample. The photolysis beam was positioned ± 80-100 μm away from the cell somata, side-by-side to a visualized dendrite. Optimization of laser photolysis was obtained by adjusting the position of the slice with respect to the laser beam, and the laser power was tuned (3-10 mW), in order to ensure that laser-evoked EPSCs yielded similar kinetics to those of synaptic EPSCs. AMPA/NMDA ratios were obtained by dividing the peak of AMPAR-EPSC (−60 mV) by the NMDAR-EPSC (+40 mV, ± 100 ms after onset when AMPAR-EPSC decayed).

Single-unit recordings under anesthesia

For the validation of rAAV$_8$-hSyn1-JAWS-GFP *in vivo*, 12 week-old mice were anesthetized with intranasal isoflurane (Univentor; 2% for induction, 1%–1.5% for maintenance) and placed onto a stereotaxic apparatus (Kopf Instruments). Their body temperature was maintained at 36°C using a feedback-controlled heating pad (CMA-450; Phymep). The scalp was retracted and a burr hole was drilled

above the LHb (AP −1.32 from bregma; ML ± 0.42; DV −2.8), for the placement of a recording electrode. Single-unit activity of spontaneous action potentials (minimal duration of recording epochs: 3 minutes), was recorded extracellularly using glass micropipettes (impedance: 5-15 MΩ), filled with 2% Chicago Sky Blue dissolved in 0.5 M sodium acetate. The signal was filtered (band-pass: 500-5000 Hz), pre-amplified (DAM80; WPI, Germany), amplified (Neurolog System; Digitimer, UK), and displayed on a digital storage oscilloscope (OX 530; Metrix, USA). Experiments were sampled online and offline by a computer connected to a laboratory interface (CED Power 1401; Cambridge Electronic Design, UK) running the Spike2 software (Cambridge Electronic Design, UK). Stable cells were subjected to 10 pulses of red light (638 nm, 8 mW, continuous light during 10 s). Raster plots and peri-stimulus time histograms were built using a bin width of 1 s.

Histology

Once the behavioral experiments were finished, animals were perfused transcardially with paraformaldehyde (4% PFA in 10 mM PBS). Brains were dissected out and kept at 4°C until slicing. A vibratome VT1000-S (Leica) was used to obtain coronal sections (100 μm). To corroborate proper fiber placement and injection site, we took images with an epi-fluorescent microscope (Zeiss). For optogenetic experiments, pictures were taken from the same slices in which electrophysiological recordings were performed.

Array tomography

Tissue preparation

7 week-old mice were anaesthetized with ketamine (150 mg/kg) and xylazine (100 mg/kg) and perfused transcardially with 4% PFA in 100 mM phosphate buffer (pH 7.4). Brains were dissected out, post-fixed in 4% PFA overnight at 4°C, and then equilibrated in 30% sucrose for 48 hours. Coronal tissue blocks containing both LHb nuclei were cut into 300 μm thick sections using a vibratome, and sections were subsequently processed for array tomography. Tissue sections were dehydrated in graded series of alcohol up to 70% ethanol (5 minutes each step at room temperature). Subsequently, the tissue was infiltrated in a 1:3 mixture of 70% ethanol and LRWhite resin (medium grade; Electron Microscopy Sciences) for 5 minutes, and then two times of 5 minutes in 100% LRWhite. The tissue was then infiltrated in LRWhite overnight at 4°C. On the following day, sections were flat-embedded between a glass slide (to provide a flat surface) and a sheet of ACLAR plastic (Electron Microcopy Sciences) to facilitate removal of the tissue section, and polymerized for 24 hours at 55°C. After embedding, the LHb was excised and mounted on EMBed blocks using a superglue for ultra-sectioning. Series of 25 100-nm sections were cut in ribbons using Jumbo Histo Diamond Knife (Diatome) and an ultra-microtome (UltraCut, Leica). The ribbons were mounted on glass coverslips coated with 0.1% gelatin and 0.01% chromium potassium sulfate, air-dried, placed on a hot plate (60°C) for 30 minutes, and then stored at room temperature until processing for immunofluorescence.

Immunofluorescence

Monoclonal antibodies were used to detect Synapsin-1 (rabbit, 1:200; Cell Signaling Technology; D12G5 XP, #5297), GluA1 (mouse, 1:200; Millipore; MAB2263, RH95) and GluN1 (mouse, 1:200; Chemicon; MAB363, 54.1). DAPI staining was included in each round for alignment purposes. Sections were then re-immunolabeled with a different set of antibodies and re-imaged in two rounds. For immunolabeling, sections were encircled with a hydrophobic barrier pen (ImmEdge, Vector Labs) and pre-incubated for 5 minutes in blocking solution (0.05% Tween, 0.1% bovine serum albumin in Tris buffer saline, pH 7.6). Subsequently, primary antibodies were diluted together in blocking solution and incubated with sections for 2 hours. Sections were thoroughly rinsed with PBS for three times, of 10 minutes each, using a plastic transfer pipette. Fluorescent-conjugated secondary antisera raised in donkey were used (anti-rabbit Alexa Fluor 647, anti-mouse Alexa Fluor 488 and anti-mouse Cy3; 1:200; Jackson ImmunoResearch). Secondary antisera were centrifuged at 13.000 rpm for 3 minutes before usage. Sections were incubated with the secondary antisera for 24 minutes and rinsed. Coverslips with sections were mounted on a glass slide using the SlowFade Gold Antifade Mountant with DAPI (Life Technologies) for imaging. After imaging, applied antibodies were eluted by incubating the sections with 0.02% SDS and 0.2 M NaOH in distilled water for 20 minutes. After two washes of 10 minutes with distilled water, coverslips were air-dried and placed on a hot plate (60°C) for 30 minutes. Upon re-immunolabeling, negative controls omitting primary antisera were run to corroborate the complete elution of primary antibodies.

Microscopy and image processing

Sections were imaged on a Leica DM6000 fluorescence microscope using an oil objective (Plan-Apochromat 63X/1.4 NA; Leica) and a CoolSNAP EZ camera. Serial images were processed, aligned and converted into stacks using Fiji software with *StackReg/MultiStackReg* plugins and DAPI staining. We analyzed 2 stacks per mouse of at least 20 images each. The quantitative analysis was done using sampling masks with average dimensions of 70 μm x 70 μm. Axon terminals were identified by the presence of Synapsin, and their relation to postsynaptic glutamate receptors was analyzed using the *Multiply* operation of the *Image Calculator* function. Resulting objects with overlapping voxels were then counted using the *Object Counter 3D* plugin, yielding density values (puncta per μm^3). Due to the high-resolution of array tomography, adjacent objects located in different synaptic compartments may not co-localize in the classic way, and their immunolabeled voxels may not overlap. To avoid these possible instances of under-detection in the quantitative analysis, we used the *Dilate* function to introduce a mask expansion in the size of one of the objects (< 0.2 μm). In the resulting dataset, we examined the presence of overlapping immunolabeled voxels. A mean density value was calculated per mouse.

QUANTIFICATION AND STATISTICAL ANALYSIS

Data analysis was performed using IGOR Pro (Wave Metrics) and Prism (GraphPad). Most data are represented using box and scatterplots depicting the median, 10%–90% confidence intervals and individual values. Correlation plots illustrate single-mouse means and, when appropriate, individual values. Results from fiber photometry are plotted on a single-mouse basis using heatmaps. For alternative plot representations, we show mean ± SEM. We employed the following statistical tests: Mann-Whitney test, Student's t test, one-way ANOVA and two-way ANOVA. Unless otherwise specified, tests are unpaired and two-tailed. *Post hoc* corrections for multiple comparisons were performed when appropriate (after one-way ANOVA and two-way ANOVA). Significance was conventionally set as ***$p < 0.001$, **$p < 0.01$ and *$p < 0.05$.

Neuron, Volume *109*

Supplemental information

Stress undermines reward-guided cognitive performance through synaptic depression in the lateral habenula

Alvaro Nuno-Perez, Massimo Trusel, Arnaud L. Lalive, Mauro Congiu, Denise Gastaldo, Anna Tchenio, Salvatore Lecca, Mariano Soiza-Reilly, Claudia Bagni, and Manuel Mameli

Nuno-Perez et al., Supplemental Figure 1

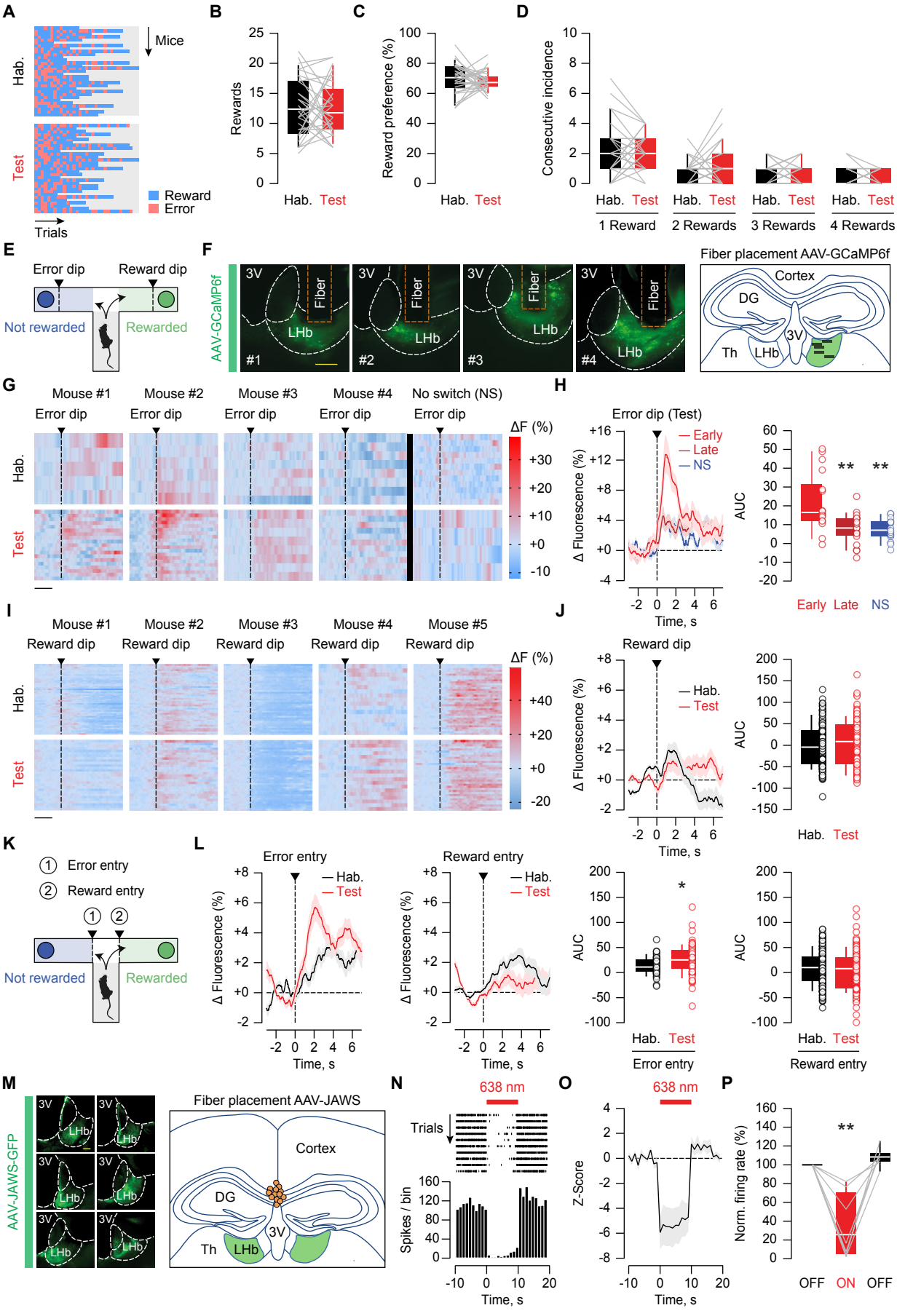

Figure S1. Behavioral, photometric and optogenetic analysis of LHb neurons during the T-maze task. Related to Figure 1.

(**A**) Single-mouse performance during habituation and test session (n=31 mice).

(**B**) Box and scatter plots of the reward incidence during habituation (black: n=31 mice, 12.74±0.8884) and test session (red: n=31 mice, 12.52±0.8137).

(**C**) Box and scatter plots of the reward preference during habituation (black: n=31 mice, 69.93±1.885) and test session (red: n=31 mice, 68.05±1.169).

(**D**) Box and scatter plots of the consecutive error incidence during habituation (black: n=31 mice, 2.0968±0.3172 for 1 error, 0.8387±0.1298 for 2 errors, 0.6774±0.1239 for 3 errors, and 0.3548±0.1075 for 4 errors) and test session (red: n=31 mice, 2.1613±0.2095 for 1 error, 1.2258±0.2268 for 2 errors, 0.5161±0.1279 for 3 errors, and 0.4194±0.0886 for 4 errors).

(**E**) Schematic of the behavioral task.

(**F**) Injection sites of AAV-GCaMP6f and fiber implantation above the site of injection (scale bar: 100 µm) in the cohort of mice employed for photometric experiments (Figure 1F). Coronal schematic depicting the approximate sites of fiber placement (black rectangles: n=5 mice).

(**G**) Single-mouse heat maps of LHb fluorescence aligned to the entry into the non-rewarded container (error dip) during habituation and test session (scale bar: 2 s).

(**H**) Time course of the average LHb fluorescence aligned to the entry into the non-rewarded container (error dip) during early and late trials of the test session, and during test trials in which the non-rewarded arm was not switched (NS). Box and scatter plots of the area under the curve (AUC) during early (light red: n=5 mice/17 trials, 21.8±3.769), late (dark red: n=5 mice/19 trials, 7.989±1.857) and no-switch trials during the test session (blue, NS: n=4 mice/15 trials, 7.274±1.517). One-way ANOVA ($F_{2,48}$=9.84) with Holm-Sidak correction (**p<0.01, comparisons against early).

(**I**) Single-mouse heat maps of LHb fluorescence aligned to the entry into the rewarded container (reward dip) during habituation and test session (scale bar: 2 s).

(**J**) Time course of the average LHb fluorescence aligned to the entry into the rewarded container (reward dip) during habituation and test session. Box and scatter plots of the area under the curve (AUC) during habituation (black: n=5 mice/186 trials, -0.3678±3.565) and test session (red: n=5 mice/149 trials, 5.404±4.376).

(**K**) Schematic of the behavioral task.

(**L**) Time course of the average LHb fluorescence during habituation and test session aligned to the entry into the non-rewarded and rewarded arms. Box and scatter plots of the area under the curve (AUC) during habituation (black: n=5 mice/46 trials, 13.6299±2.6152 for entry into non-rewarded arm; n=5 mice/186 trials, 10.1795±2.4401 for entry into rewarded arm) and test session (red: n=5 mice/74 trials, 25.0754±3.4268 for entry into non-rewarded arm; n=5 mice/150 trials, 4.3685±3.1677 for entry into rewarded arm). Mann-Whitney test (U=1228, *p<0.05).

(**M**) Representative injection sites of AAV-JAWS (scale bar: 100 µm) in the cohort of mice employed for behavioral experiments (Figure 1I). Coronal schematic depicting the approximate sites of fiber placement for the optical activation of JAWS (orange circles: n=13 mice).

(**N**) Raster plot and peri-stimulus time histogram of an example LHb neuron for the *in vivo* validation of JAWS photoactivation.

(**O**) Time course of the average z-score of spontaneous firing activity during red light treatment (n=2 mice/7 cells).

(**P**) Box and scatter plots of the normalized firing rate during (red: ON, 34.7±13.21) and after (black: OFF, 108.6±3.782) red light treatment (n=2 mice/7 cells). One-way repeated measures ANOVA ($F_{1.096,6.574}$=24.37) with Holm-Sidak correction (**p<0.01, ON versus OFF).

Data are represented with heat maps, box plots (median and quartiles) or mean±SEM.

Nuno-Perez et al., Supplemental Figure 2

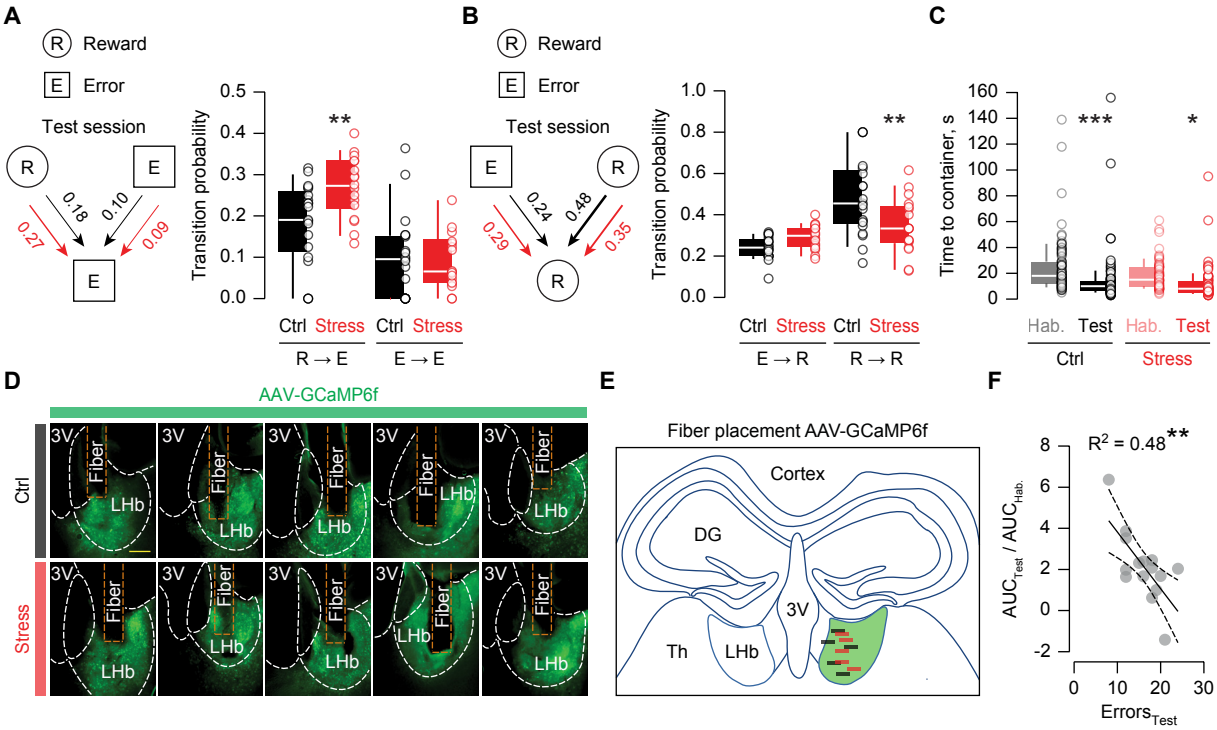

Figure S2. Behavioral and photometric analysis upon stress exposure. Related to Figure 2.

(**A**) Diagram displaying average transition probabilities to error choice during the test session. Box and scatter plots of transition probabilities to error choice in control (black: n=20 mice, 0.1817±0.02232 for R→E and 0.0973±0.02289 for E→E) and stressed mice (red: n=17 mice, 0.27±0.01914 for R→E and 0.08755±0.01605 for E→E). Two-way repeated measures ANOVA ($F_{1,35}$=3.214) with Sidak correction (**p<0.01, control versus stress).

(**B**) Diagram displaying average transition probabilities to reward choice during the test session. Box and scatter plots of transition probabilities to reward choice in control (black: n=20 mice, 0.241±0.01213 for E→R and 0.48±0.04154 for R→R) and stressed mice (red: n=17 mice, 0.2937±0.01448 for E→R and 0.3487±0.03276 for R→R). Two-way repeated measures ANOVA ($F_{1,35}$=3.214) with Sidak correction (**p<0.01, control versus stress).

(**C**) Box and scatter plots of the time to reach the arm containers in control (black: n=20 mice/100 trials, 23.87±2.015 during habituation; n=20 mice/100 trials, 13.56±1.877 during test) and stressed mice (red: n=15 mice/75 trials, 18.16±1.283 during habituation; n=17 mice/84 trials, 11.36±1.351 during test). Two-way ANOVA ($F_{1,355}$=23.7) with Sidak correction (***p<0.001, *p<0.05, habituation versus test).

(**D**) Injection sites of AAV-GCaMP6f and fiber implantation above the site of injection (scale bar: 100 µm) in the cohort of mice employed for photometric experiments (Figure 2C).

(**E**) Coronal schematic depicting the approximate sites of fiber placement (control: black rectangles, n=5 mice; stress: red rectangles, n=5 mice).

(**F**) Correlation plot between error incidence during the test session and LHb fluorescence aligned to the entry into the non-rewarded container (n=15 mice: 5 naïve mice from Figure 1F, 5 control mice from Figure 2C and 5 stressed mice from Figure 2C). Pearson correlation (R^2=0.4842, $F_{1,13}$=12.21, **p<0.01).

Data are represented with box plots (median and quartiles) or mean±SEM.

Nuno-Perez et al., Supplemental Figure 3

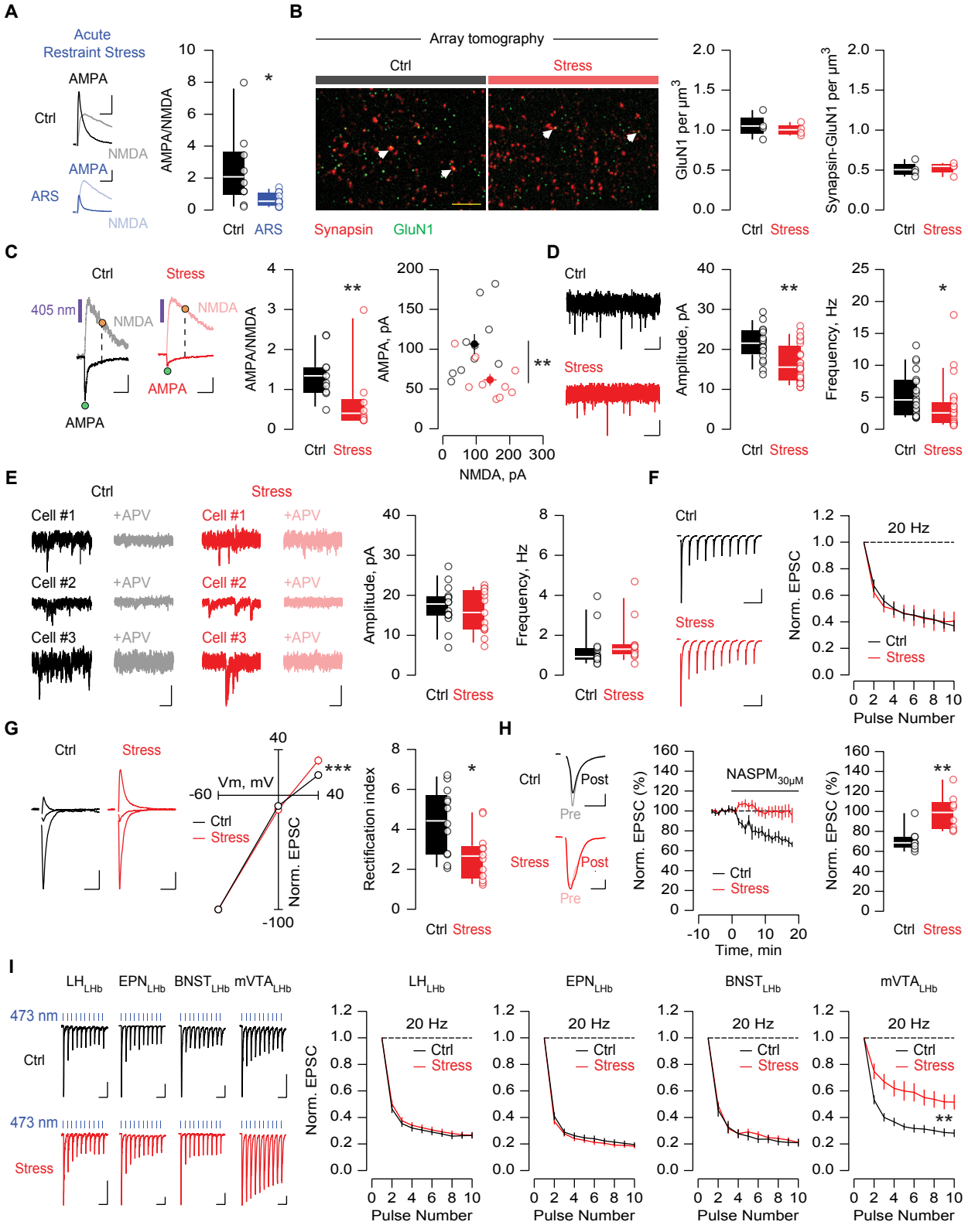

Figure S3. Stress reduces habenular AMPAR transmission. Related to Figure 2 and Figure 3.

(**A**) Example traces of AMPA/NMDA (+40 mV; scale bars: 50 pA, 10 ms). Box and scatter plots of AMPA/NMDA from control (black: n=2 mice/9 cells, 2.51±0.8158) and restrained mice (ARS, blue: n=3 mice/11 cells, 0.6564±0.1283). Mann-Whitney test (U=19, *p<0.05).

(**B**) Array tomography images obtained from single 100-nm slices immunolabeled against Synapsin (red) and GluN1 (green) (scale bar: 5 µm). White arrows indicate representative puncta showing co-localization of both markers. Box and scatter plots of the number of puncta per μm^3 in control (black: n=4 mice, 1.053±0.07596 for GluN1 and 0.5085±0.04607 for Synapsin/GluN1) and stressed mice (red: n=4 mice, 1.004±0.03689 for GluN1 and 0.5245±0.03795 for Synapsin/GluN1).

(**C**) Example traces of AMPA/NMDA with single-photon MNI-glutamate uncaging (-60/+40 mV; scale bars: 50 pA, 100 ms). Box and scatter plots of AMPA/NMDA from control (black: n=3 mice/10 cells, 1.372±0.1917) and stressed mice (red: n=2 mice/9 cells, 0.7061±0.2958). Scatter plot of absolute amplitudes in control (black: 106.4±13.28 for AMPAR and 94.29±15.79 for NMDAR) and stressed mice (red: 61.46±7.942 for AMPAR and 141.1±20.67 for NMDAR). Mann-Whitney test (U=13, **p<0.01).

(**D**) Example traces of AMPAR-mediated miniature EPSC recordings (mEPSC; -60 mV; scale bars: 10 pA, 250 ms). Box and scatter plots of mEPSC amplitude and frequency from control (black: n=3 mice/19 cells, 21.39±0.9497 for amplitude and 5.403±0.817 for frequency) and stressed mice (red: n=3 mice/23 cells, 16.5±1.003 for amplitude and 3.557±0.8387 for frequency). Mann-Whitney test (amplitude: U=98; frequency: U=127) (**p<0.01, *p<0.05).

(**E**) Example traces of NMDAR-mediated spontaneous EPSC recordings (sEPSC; -60 mV; scale bars: 20 pA, 100 ms), before and after bath application of the NMDAR antagonist APV. Box and scatter plots of sEPSC amplitude and frequency from control (black: n=2 mice/15 cells, 17.39±1.33 for amplitude and 1.279±0.2438 for frequency) and stressed mice (red: n=2 mice/13 cells, 15.8±1.495 for amplitude and 1.593±0.3034 for frequency).

(**F**) Example traces of AMPAR EPSC trains (-50 mV; scale bars: 50 pA, 100 ms). Plot of normalized EPSC amplitudes from control (black: n=2 mice/12 cells) and stressed mice (red: n=2 mice/12 cells).

(**G**) Example traces of AMPAR currents (-60/+0/+40 mV; scale bars: 50 pA, 10 ms). Current-voltage relationship, box and scatter plots of rectification index from control (black: n=2 mice/12 cells, 4.422±0.4847) and stressed mice (red: n=2 mice/12 cells, 2.663±0.359). Two-way repeated measures ANOVA ($F_{1,22}$=2.693) with Sidak correction (***p<0.001); Mann-Whitney test (U=28, *p<0.05).

(**H**) Example traces of AMPAR currents (-50 mV; scale bars: 50 pA, 5 ms). Time course, box and scatter plots of the NASPM sensitivity (30 µM) of AMPAR currents from control (black: n=3 mice/8 cells, 71.5±4.241) and stressed mice (red: n=3 mice/8 cells, 98.88±6.391). Mann-Whitney test (U=4, **p<0.01).

(**I**) Example traces of input-specific (Channelrhodopsin-2) AMPAR EPSC trains (-60 mV; scale bars: 50 pA, 100 ms). Plots of normalized EPSC amplitudes from control (black: LH, n=2 mice/24 cells; EPN, n=2 mice/29 cells; BNST, n=4 mice/34 cells; mVTA, n=2 mice/32 cells) and stressed mice (red: LH, n=3 mice/33 cells; EPN, n=2 mice/27 cells; BNST, n=2 mice/23 cells; mVTA, n=3 mice/43 cells). Two-way repeated measures ANOVA ($F_{1,73}$=10.59, **p<0.01, control versus stress interaction).

Data are represented with box plots (median and quartiles) or mean±SEM.

Nuno-Perez et al., Supplemental Figure 4

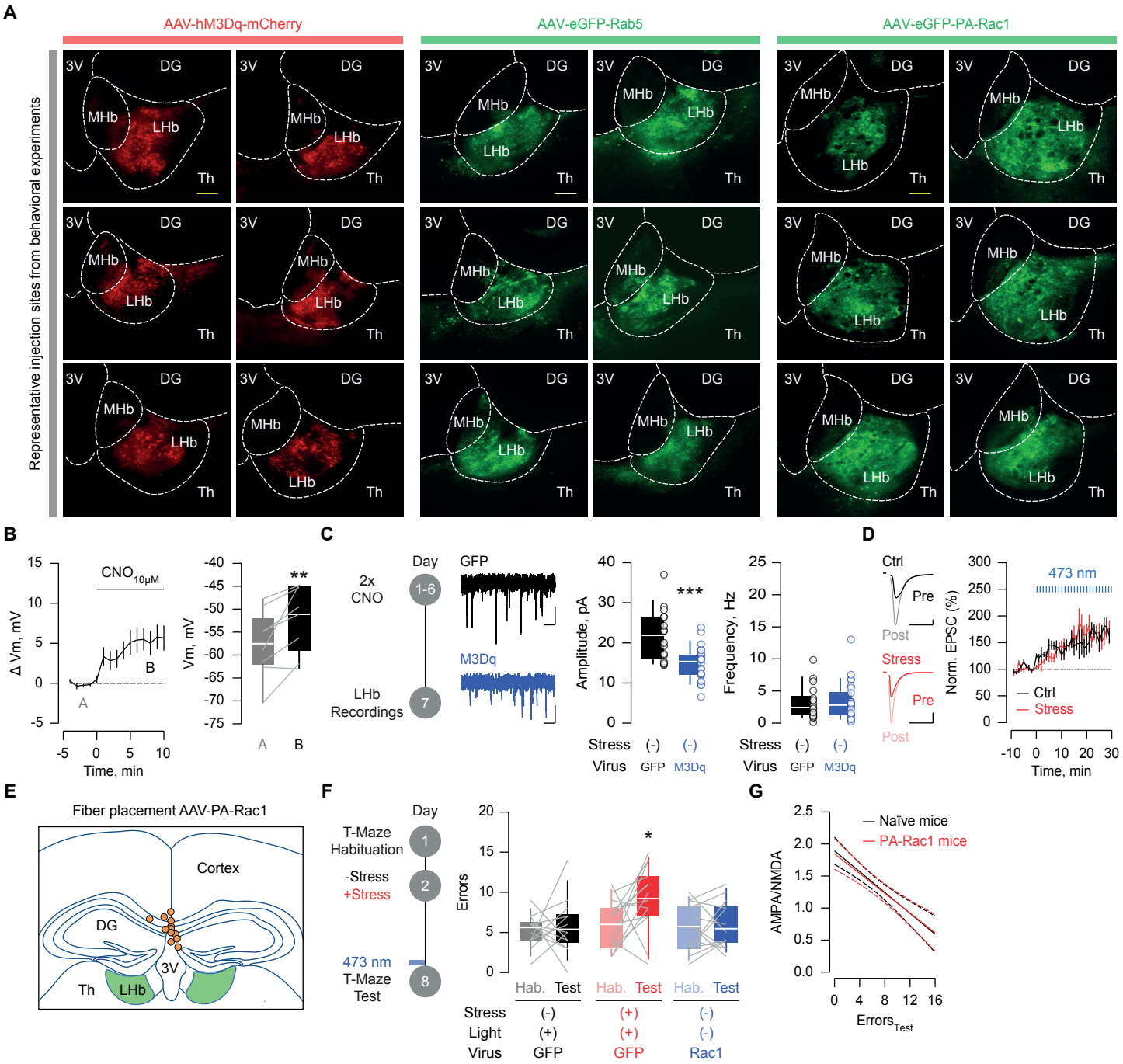

Figure S4. Validation of viral manipulations. Related to Figure 4.

(**A**) Representative injection sites of AAV-hM3Dq (scale bar: 100 μm), AAV-Rab5 (scale bar: 100 μm) and AAV-PA-Rac1 (scale bar: 50 μm) in the cohort of mice employed for behavioral experiments (Figure 4C, 4F and 4H).

(**B**) Time course of the change in membrane potential in LHb neurons upon bath application of CNO (10 μM). Box and scatter plots of the membrane potential before (grey: A, -57.53±2.643) and after (black: B, -52.06±2.654) CNO treatment (n=3 mice/8 cells). Paired student's t-test (t_7=3.536, **p<0.01).

(**C**) Experimental timeline. Example traces of AMPAR-mediated miniature EPSC recordings (mEPSC; -60 mV; scale bars: 10 pA, 250 ms). Box and scatter plots of mEPSC amplitude and frequency from GFP (black: n=2 mice/16 cells, 21.84±1.615 for amplitude and 3.097±0.6359 for frequency) and M3Dq mice (blue: n=3 mice/25 cells, 14.81±0.8312 for amplitude and 3.344±0.5879 for frequency). Mann-Whitney test (U=76, ***p<0.001).

(**D**) Example traces of AMPAR currents during the *ex vivo* validation of PA-Rac1 photoactivation (-60 mV; scale bars: 50 pA, 10 ms). Time course of the amplitude of AMPAR currents from control (black: n=2 mice/9 cells) and stressed mice (red: n=2 mice/7 cells), before and after blue light delivery (1 Hz, 150 ms). Two-way repeated measures ANOVA ($F_{38,532}$=6.577, ***p<0.001, time interaction).

(**E**) Coronal schematic depicting the approximate sites of fiber placement for the optical activation of PA-Rac1 (orange circles: n=12 mice).

(**F**) Experimental timeline. Box and scatter plots of the error incidence in GFP mice subjected to control/light (black: n=13 mice, 5.2308±0.5456 during habituation and 5.7692±0.9176 during test), GFP mice subjected to stress/light (red: n=14 mice, 5.9286±0.7657 during habituation and 9.2143±1.0747 during test) and PA-Rac1 mice subjected to control/no-light (blue: n=13 mice, 5.4615±0.7966 during habituation and 5.9231±0.7879 during test). Two-way repeated measures ANOVA ($F_{1,37}$=3.952) with Sidak correction (*p<0.05, habituation versus test).

(**G**) Overlay of the correlation analysis between error incidence and AMPA/NMDA from naïve (black, Figure 1J: R^2=0.833, $F_{1,9}$=44.89, ***p<0.001) and stressed PA-Rac1 mice (red, Figure 4I: R^2=0.9388, $F_{1,4}$=61.38, **p<0.01). Pearson correlation with test for slope comparison ($F_{1,13}$=0.06798, p=0.7984).

Data are represented with box plots (median and quartiles) or mean±SEM.